1 **Paleocene-Eocene age glendonites from the Norwegian Margin -**

2 **Indicators of cold snaps in the hothouse?**

3 Madeleine L. Vickers[1*], Morgan T. Jones[1], Jack Longman[2], David Evans[3,4,†], Clemens V. Ullmann[5], Ella

4 Wulfsberg Stokke[1], Martin Vickers[6], Joost Frieling[7], Dustin T. Harper[8], Vincent J. Clementi[9] & IODP

5 Expedition 396 Scientists[10]

6 [1] Centre for Planetary Habitability (PHAB), University of Oslo, P.O. Box 1028 Blindern, 0315 Oslo, Norway

7 [2] Department of Geography and Environmental Sciences, Northumbria University, Newcastle-upon-Tyne, UK

8 [3] Institute of Geosciences, Goethe University Frankfurt, Altenhöferallee 1, 60438 Frankfurt am Main, Germany

9 [4] FIERCE, Frankfurt Isotope & Element Research Center, Goethe University Frankfurt, Altenhöferallee 1, 60438 Frankfurt am

10 Main, Germany

11 [5] Camborne School of Mines, University of Exeter, Penryn Campus, Penryn TR10 9FE, UK

12 [6] Department of Chemistry, UCL, 20 Gordon Street, London WC1H 0AJ, UK

13 [7] Department of Earth Sciences, University of Oxford, Oxford, United Kingdom

14 [8] University of Utah, Dept. of Geology & Geophysics, 115 S 1460 E, Salt Lake City, UT 84112, U.S.A.

15 [9] Department of Marine and Coastal Sciences, Rutgers University, New Brunswick, NJ 08901, U.S.A.

16 [10] Expedition 396 shipboard scientists as listed in Preliminary Report - Planke, S., Berndt, C., & Zarikian, C. A. A. (2022).

17 *m.l.vickers@geo.uio.no

18 [†] Now at: School of Ocean and Earth Science, University of Southampton, Southampton, SO14 3ZH, UK

19 **Abstract**

20 The International Ocean Discovery Program (IODP) Expedition 396 to the mid-Norwegian margin

21 recovered >1300 m of pristinely preserved, volcanic ash-rich sediments deposited during the late

22 Paleocene and early Eocene, from close to the centre of the North Atlantic Igneous Province (NAIP).

23 Remarkably, many of these cores contain glendonites, pseudomorphs after the purported cold-water

24 mineral ikaite, from sediments dated to the late Paleocene, Paleocene – Eocene boundary and early

25 Eocene. These time intervals span some of the hottest climates of the Cenozoic, including the

26   Paleocene-Eocene Thermal Maximum (PETM). Global deep ocean temperatures are not thought to

27   have dropped below 10 °C at any point during this time, making the occurrence of supposedly cold-

28   water (near-freezing temperature) glendonite pseudomorphs seemingly paradoxical. This study

29   presents a detailed sedimentological, geochemical, and microscopic study of the Exp. 396 glendonites,

30   and presents an updated model for the ikaite-to-calcite transformation for these glendonites.

31   Specifically, we show that early diagenesis of basaltic ashes of the NAIP appear to have chemically

32   promoted ikaite growth in the sediments in this region. Together with existing knowledge of late

33   Paleocene and early Eocene glendonites from Svalbard to the north, and early Eocene glendonites

34   from Denmark to the south, these new glendonite finds possibly imply episodic, short-duration, and

35   likely localised cooling in the Nordic Seas region, which may have been directly or indirectly linked to

36   the emplacement of the NAIP.

37   **1. Introduction**

38   Glendonites are pseudomorphs after the mineral ikaite, a metastable, hydrated form of calcium

39   carbonate ($CaCO_3 \cdot 6H_2O$), which is found today growing in a range of environments (alkaline lakes, sea

40   ice, concrete, in estuarine settings, deep marine sediments and more; Council and Bennet, 1993;

41   Buchardt et al., 2001; Dieckmann et al., 2008; Boch et al., 2015; Zhou et al., 2015; Schultz et al., 2022;

42   2023). Certain physical and chemical conditions are necessary in order for ikaite to precipitate

43   preferentially over the more stable anhydrous $CaCO_3$ polymorphs (calcite, aragonite, vaterite). These

44   parameters may include low temperatures, high alkalinity, and a range of possible chemical inhibitors

45   of the anhydrous polymorphs (e.g. high aqueous Mg, phosphate, and/or sulphate concentrations;

46   certain dissolved organic compounds) (Council and Bennett, 1993; Buchardt et al., 2001; Zhou et al.,

47   2015; Purgstaller et al., 2017; Stockmann et al., 2018; Whiticar et al., 2022). Whilst laboratory studies

48   have successfully, if fleetingly, precipitated ikaite at warm temperatures (≤ 35 °C), temperatures

49   approaching zero are much more favourable for the precipitation, growth, and longevity of this

50   mineral (Purgstaller et al., 2017; Stockmann et al., 2018; Tollefsen et al., 2020). In nature, ikaite has

51   not been discovered growing above 7 °C (Suess et al., 1982; Dieckmann et al., 2008; Zhou et al., 2015;

52   Boch et al., 2015; Stockmann et al., 2022).

53   Glendonites are found throughout the geological record in marine sedimentary settings, sometimes

54   associated with glacial deposits (e.g. Kemper, 1987; Alley et al., 2020), in sediments deposited during

55   periods of both icehouse and greenhouse climate (Rogov et al., 2021; 2023). The occurrence of

56   glendonites in Mesozoic marine sediments has fuelled the debate about whether ephemeral polar ice

57   sheets waxed and waned during this long-term global greenhouse climate (e.g. Kemper, 1987; de Lurio

58   and Frakes, 1999; Rogov et al., 2017; Vickers et al., 2019; Merkel and Munnecke, 2023). Across the

59   Cenozoic sedimentary record, glendonites are found at increasingly broader latitude ranges through

60   time, coincident with the growth of polar ice caps and global climate cooling (Rogov et al., 2021).

61   However, reports of glendonites – including the largest ever discovered on Earth – from successions

62   deposited in the Nordic Seas region during the early Paleogene greenhouse have been a topic of

63   controversy in the paleoclimate community (Huggett et al., 2005; Spielhagen and Tripati, 2009). Deep

64   ocean bottom water temperatures were >10 °C across the globe, including the North Atlantic, during

65   much of the Paleocene and Early Eocene (Zachos et al., 2008; Dunkley-Jones et al., 2013; Westerhold

66   et al., 2020; Meckler et al. 2022), such that the presence of glendonites in marine sedimentary

67   sequences during this time appears paradoxical. Whilst the successful synthesis of ikaite at warm (≤

68   35 °C) temperatures in laboratory conditions raises the possibility of ikaite/glendonite formation at

69   much warmer temperatures than modern-day natural ikaites (Tollefsen et al., 2020), the conditions

70   under which this was achieved in the laboratory is unlike any natural setting. In addition, clumped

71   isotope temperature reconstructions for ikaite precipitation/transformation temperatures from a

72   Danish early Eocene succession suggest cold formation (or perhaps transformation) conditions for the

73   parent ikaite (0 - 9 °C) (Vickers et al., 2020). Given that the parent ikaite minerals grew from pore

74   waters in the shallow subsurface (e.g., Zhou et al., 2015; Schultz et al., 2022), this suggests that local

75   bottom water temperatures must have been at least this cold (Vickers et al., 2020), since temperature

76   increases with burial depth. Reconstructed sea surface temperatures from biomarkers for northern

77   Denmark also suggest that short-term cooling events of magnitude c. 5 - 7 °C may have punctuated

78   the late Paleogene to early Eocene (summarised in Jones et al., 2023). Whether these cooling events

79   reflect a localised as well as short-lived cooling is not understood, nor the mechanism by which such

80   cooling could occur, although these have been speculated upon (Schoon et al., 2015; Stokke et al.,

81   2020a; Vickers et al., 2020).

82   International Ocean Discovery Program (IODP) Expedition 396 to the Norwegian continental margin

83   (August – September 2021) recovered numerous glendonites in volcanic sediments dated as latest

84   Paleocene and earliest Eocene, including, remarkably, within those sediments deposited during the

85   Paleocene-Eocene Thermal Maximum (PETM) hyperthermal event (Berndt et al., 2023; Planke et al.,

86   2023). Deep ocean bottom water temperatures may have reached 15 °C or more during the 150 – 200

87   kyr-long PETM hyperthermal (Röhl et al., 2007; Zachos et al., 2008; Murphy et al., 2010; Dunkley Jones

88   et al., 2013; Westerhold et al., 2020). This makes the discovery of pseudomorphs after a mineral

89   favoured by near-freezing conditions truly remarkable if the age of their formation and

90   recrystallisation coincided with the depositional age of the host sediments. If the parent ikaite grew

91   during the PETM or the hothouse earliest Eocene climate (e.g. as was the case for the well-studied Fur

92 Formation glendonites; Vickers et al., 2020), this raises questions about regional seaway connectivity,

93 thermal stratification in both the Nordic Seas and the open oceans, and could imply that current global

94 and regional temperature reconstructions based on biogenic carbonates and lipid biomarkers do not

95 represent the full spectrum of climate variability in the early Paleogene Northern Hemisphere.

96 This study documents and describes the glendonites in the stratigraphy of the Exp. 396 cores, and uses

97 microscopic and geochemical analyses along with sedimentological data to elucidate the timing,

98 climate, and chemical regimes that facilitated their formation.

99 **2. Materials and Methods**

100 *2.1 Geological setting and sampling*

101 IODP Expedition 396 drilled 21 boreholes along the mid-Norwegian continental margin during August

102 and September 2021, recovering igneous and sedimentary rocks ranging from lava flow fields to

103 hydrothermal vent complexes, including thick successions of upper Paleocene and lower Eocene strata

104 (Fig. 1A). Ship-board sedimentary logging was followed by a more detailed high-resolution study of

105 recovered cores stored at MARUM, Bremen, under refrigerated conditions (c. 4 °C). Two transects

106 sampled Paleocene-Eocene sedimentary successions at the Modgunn and Mimir localities (Fig. 1B and

107 C).

108 The Modgunn locality is a transect of boreholes (Sites U1567-U1568) that span the crater of a

109 Paleogene hydrothermal vent complex close to the rift axis of the Møre Margin (Fig. 1B; Planke et al.,

110 2023). These vents formed due to the violent expulsion of volatiles generated by contact

111 metamorphism of organic-rich sediments around igneous intrusions, and from magmatic degassing

112 (e.g. Svensen et al., 2004). The Modgunn crater is approximately 80 m deep compared to the paleo-

113 seafloor, with a 200-240m-wide feeder system that is rooted in a series of nested sill intrusions (Berndt

114 et al., 2023). The vent infill consists predominantly of laminated diatom-rich mud, mudstones, and ash

115 layers that rapidly accumulated to fill the bathymetric depression. The strata contain a negative δ^{13}C

116 excursion and the biostratigraphic marker taxa *Apectodinium augustum* and *Hemiaulus proteus*. Based

117 on these biostratigraphic and chemostratigraphic constraints, Berndt et al. (2023) showed the vent

118 formed just before the PETM onset and was completely filled within the duration of the PETM CIE.

119 The Mimir High (Sites U1569-U1570) is a borehole transect through a marginal high on the Vøring

120 Transform Margin (Fig. 1C; Planke et al., 2023). Uplift and erosion of the marginal high has removed

121 any basalt cover (Berndt et al., 2001), providing a window to access stratigraphic successions below

122   the breakup volcanism. The strata dip to the north, so a transect of boreholes was designed to provide

123   a composite late Paleocene – early Eocene section with overlap between each hole. These strata

124   consist of a mix of mud, mudstones, carbonates, igneous units, and ash layers (Planke et al., 2023).

125   Core sampling, including sampling the glendonites, was undertaken in April 2022 and high-resolution

126   sediment logging of the glendonite-bearing core sections was undertaken in August 2022, at MARUM,

127   University of Bremen, Germany.

128   *2.2 Powder X-Ray Diffraction (PXRD)*

129   Powder X-ray diffraction (PXRD) was carried out on dried, powdered bulk sub-samples of five

130   glendonites from the Exp. 396 cores, using a Stoe StadiP transmission (thin-foil) diffractometer with a

131   copper anode at 30 mA, 40 kV and a germanium 111 monochromator to produce $K\alpha1$ X-rays. The

132   diffracted beam was collected by an 18° 2θ Dectris Mythen1K silicon strip detector. Samples were

133   sandwiched between two thin cellulose acetate discs and mounted in a holder set to spin continuously

134   during data collection. Data sets were scanned from 5 to 65° 2θ stepping at 0.5° and 20 s/step. The

135   resultant raw data has a step of 0.015° 2θ. Machine alignment was monitored using an NBS silicon

136   standard. Phase analysis was undertaken using Bruker's 'Eva' program (Gates-Rector and Blanton,

137   2019) interfaced with the Powder Diffraction File provided by the International Centre for Diffraction

138   Data.

139   *2.3 Microscopy*

140   Four polished thin sections were made from three glendonites (those in U1569A-19R-2, U1570A-15R-

141   1, and U1567C-11X-1), and examined using a light microscope to compare to published data on

142   glendonite microfabric and look for different carbonate growth phases. A Hitachi SU5000 FE-SEM,

143   equipped with a Bruker EDS was used to examine porosity and spatial chemical variation across the

144   sub-samples.

145   *2.4 Laser Ablation Inductively Coupled Plasma Mass Spectrometry (LA ICP-MS)*

146   Laser ablation trace element analyses were performed on polished thin sections of glendonites from

147   U1569A-19R-2, U1570A-15R-1, and U1567C-11X-1 at the Frankfurt Isotope and Element Research

148   Center (FIERCE) in the Institute of Geosciences at Goethe University Frankfurt. Different carbonate

149   phases were targeted. The system features a 193 nm RESOlution M-50 laser ablation (LA) system with

150   two-volume LaurinTechnic ablation cell connected to a ThermoScientific Element XR sector field

151   inductively coupled plasma mass spectrometer (ICP-MS). All analyses were performed as 'spot'

152   measurements, utilising relatively low repetition rates to ablate through the thin sections analysed

153   here. Ablation took place with He in the outer cell (400 ml/min) and Ar sample gas from the ICP-MS

154   (1.025 l/min) mixed into the lower-volume inner cell. N_2 was admixed downstream of the ablation cell

155   (4.5 ml/min) to improve sensitivity (e.g. Durrant, 1994). The ICP-MS was fitted with a Ni jet sample

156   cone and Ni H skimmer cone and operated in medium resolution mode. Tuning of the system was

157   performed to maximise sensitivity (~6 M cps ^{238}U in low resolution mode; NIST SRM612 60 µm, 6 Hz,

158   6 J/cm^2) while maintaining the oxide and doubly charged production rate below 0.5% and 2%

159   respectively. Monitored masses included ^{11}B, ^{23}Na, ^{24}Mg, ^{25}Mg, ^{27}Al, ^{39}K, ^{55}Mn, ^{56}Fe, ^{88}Sr, ^{138}Ba, ^{208}Pb,

160   and ^{238}U.

161   Samples were ablated using a 50 µm diameter laser beam at 4 Hz with an on-sample fluence of 5

162   J/cm^2. Quantification was performed using ^{43}Ca as the internal standard and NIST SRM610 as the

163   external standard. Data processing was performed using an in-house Matlab script following

164   established procedures (Heinrich et al., 2003), described in detail elsewhere (Evans and Müller, 2018).

165   Briefly: all analyses were baseline corrected by subtracting the mean of the two adjacent gas-blank

166   datasets, normalised to ^{43}Ca, and standardised into element/Ca molar ratios using the analyte/^{43}Ca

167   count/concentration ratio from NIST SRM610. No significant drift in this count ratio was observed for

168   any relevant analyte for the session reported here such that standardisation was based on the mean

169   of all available NIST analyses. Down-hole elemental fractionation relative to Ca was corrected by

170   calculating least-squares 3rd-order polynomials through the NIST SRM610 element/^{43}Ca-depth data,

171   which were then used as the sweep-time specific ratios for sample quantification. The NIST SRM610

172   values of Jochum et al. (2011) were used in all cases except Mg, for which we use that of Pearce et al.

173   (1997) following the data analysis of Evans and Müller (2018).

174   Data quality was assessed via repeat analysis of the 'nanopellet' version of the CaCO$_3$ standards JCp-1

175   and MACS-3 (Garbe-Schönberg and Müller, 2014; Jochum et al., 2019), ablated in an identical manner

176   to the samples. Pooling together all analyses on both standards (n = 20) and comparing to the reported

177   values of Jochum et al. (2019) yields an accuracy of <5% for ^{11}B, ^{56}Fe, ^{88}Sr, <10% for ^{23}Na, $^{24+25}$Mg, ^{138}Ba,

178   ^{238}U, 25% for ^{27}Al, 30% for ^{39}K, and 70% in the case of ^{55}Mn, comparable to the achievable long-term

179   data quality from a similar system (Evans and Müller, 2018, albeit using a quadrupole ICP-MS).

180   Precision (repeatability), defined as the 2SD of all individual analyses normalised to the reported value

181   was better than 10% in the case of ^{11}B, ^{23}Na, ^{88}Sr, ^{238}U, <15% for $^{24+25}$Mg, ^{39}K, ^{56}Fe, ^{138}Ba, 45% for ^{27}Al,

182   and 130% for ^{55}Mn. We stress that all of these values are strongly concentration-dependent and may

183   under/overestimate sample data quality depending on the analyte concentration of a given sample

184   analysis.

185   *2.5 Inductively Coupled Plasma Optical Emission Spectrometry (ICP-OES)*

186   Minor element analyses for Mg, Sr, Na, Mn, Fe, S, P, Al and Rb were undertaken on selected

187   subsamples of dried, powdered, bulk glendonites using an Agilent 5110 VDV ICP-OES at the Camborne

188   School of Mines, University of Exeter, following the method detailed in Ullmann et al. (2020). The

189   minor element data are expressed as ratios to Ca and calibrated using certified single-element

190   standards mixed to match the chemical composition of the analysed samples. Precision and accuracy

191   of the analyses were measured and controlled by interspersing multiple measurements of

192   international reference materials, JLs-1 and quality control solutions (BCQ2 and BCQ3). Analytical

193   uncertainty of element/Ca ratios in these reference materials is less than 1 % (2 RSD) at concentrations

194   > 100 times the quantification limit (measured as 6 SD of the variability of blank solutions in a batch

195   run, n = 5). For lower concentrations, the uncertainty of individual measurements is similar to the

196   quantification limit, i.e. 6 µmol/mol for Mg/Ca, 0.2 µmol/mol for Sr/Ca, 0.02 mmol/mol for Na/Ca, 5

197   µmol/mol for Mn/Ca, 5 µmol/mol for Fe/Ca, 0.2 mmol/mol for S/Ca, 0.08 mmol/mol for P/Ca, 0.06

198   mmol/mol for Al/Ca, and 0.04 mmol/mol for Rb/Ca.

199   *3.6 Microprobe data, IODP Exp. 396 ashes*

200   A representative selection (n=13) of Exp. 396 ashes from holes U1567A, U1567C, U1568A, U1568B,

201   U1569A, and U1570D were analysed for their major element composition. Individual silicate glass

202   grains were picked and mounted in epoxy for matrix glass analysis. Polished and carbon coated grain

203   mounts were analysed on a Cameca SX100 electron microprobe with 5 wavelength dispersive

204   spectrometers (WDS) at University of Oslo. Analyses were conducted with an accelerating voltage of

205   15 kV and a 10 nA beam current using a defocused beam size of 10 µm. Counting times were 10 s for

206   Na, Si, Cl, K, S, Fe, Al, Mg, and Mn; and 20 for Ca and Ti.

207   *3.7 PHREEQC modelling*

208   The PHREEQC model (version 3; Parkhurst and Appelo, 2013) was used to calculate pore water

209   chemical speciation and saturation indices for Hole U1568A, based on multiple shipboard analyses of

210   interstitial water (Planke et al., 2023). Total alkalinity and pH were measured using an autotitrator,

211   and salinity using a refractometer (Planke et al., 2023). Selected anions (SO_4^{2-}, Br^-, and Cl^-) were

212   analysed using an ion chromatograph (IC), phosphate (PO_4^{3-}) and ammonium (NH_4^+) by

213   spectrophotometry, and a range of cations using inductively coupled plasma–atomic emission

214   spectrometry (ICP-AES) (Exp. 396 Methods, Planke et al., 2023). Several cations were also measured

215   using IC that showed a good correlation with the values obtained by ICP-AES, but the model input

216   values were those from the ICP-AES for consistency. The *in situ* pressures (in atm; 1 atm = 101 kPa)

217   were estimated using the measured water depth of 1707.4 m below surface (mbsl) and a pressure

218   gradient of 0.1 atm/m in the water column. In the subsurface, a pressure gradient of 0.2 atm/m was

219   assumed, giving a pressure of 209 atm at the deepest interstitial water sample depth (192.4 m). The

220   PHREEQC model was run as a batch reactor for each solution, such that pH and pe were recalibrated

221   based on the chemical information available.

222

223   **3. Results**

224   *3.1 Sedimentological context and hand sample description*

225   The glendonites discovered by IODP Expedition 396 are found within several holes of the Modgunn

226   (U1567C and U1568B) and Mimir (U1569A and U1570A) transects (Fig. 2 and Table 1). For the

227   Modgunn transect, the glendonites are all found within the latest Paleocene and PETM-aged

228   hydrothermal vent infilling sediments (Unit IV, Fig. 2), in horizons with the most numerous and thickest

229   ash intervals (Fig. 2). Lithological Unit IV is described as "Dark greenish grey to very dark grey claystone

230   to siltstone, with common volcanic ash beds and light bioturbation" (Planke et al., 2023, p.10 Sites

231   U1567 & U1568). The glendonites in the Mimir cores are found in early Eocene-aged parts of the

232   succession, in Unit Va and Vb of U1570A, also in close association with numerous and thick ash layers.

233   In U1569A the glendonites are found at the very top of Unit Va, some 17 m above the thickest and

234   most numerous ash horizons, although notably in an interval with limited core recovery (Fig. 2), which

235   implies that these sediments may be extremely rich with unconsolidated ash horizons. The sediments

236   of Lithological Unit Va are described as "very dark grey mudstone with sparse parallel lamination and

237   slight bioturbation, with rare limestone intervals and common ash beds"; and those of Vb as "very

238   dark grey mudstone with sparse parallel lamination and slight bioturbation, with common ash beds

239   and diagenetic pyrite." (Planke et al., 2023, p10 Sites U1569 & U1570). High-resolution logs (5-cm

240   scale) of the glendonite-bearing core sections and photographs of the *in situ* glendonites can be found

241   in the Supplementary Material.

242   *3.2 Glendonite morphology*

243   The glendonites are variable in size and appearance, with some being cemented or partially cemented

244   (Fig. 3C and F), and some present as an uncemented mush of smaller crystals (Fig. 3A,B,D,E). In some

245   cases, the crystal appears to have grown over and incorporated parts of the host sediment (Fig. 3F),

246   yet in others appears to have either displaced the sediment it was growing in (Fig. 3E), or grew up into

247   the water column with later sedimentation burying it (Fig. 3C). Most show the characteristic shape of

248   stellate or bladed 'crystals', although the individual blades are no longer a single crystal but rather a

249   heterogeneous mix of smaller crystals (Fig. 3). They are generally pale beige to brown in colour,

250   although cemented examples show distinct areas within a cut 'crystal' of grey or white-pale brown

251   carbonate (Fig. 3C,F). Some samples are only small fragments of glendonite, identified by their

252   characteristic bladed shape (e.g. Fig. 3A) and/or the open, porous texture of the carbonate (e.g. Fig.

253   3D). Most of the glendonites are found *in situ*, with the exception of sample U1567C-10X-3, where

254   glendonite fragments were identified entrained in the drill mud (Fig. 3A). Therefore, these fragments

255   could have originated from some short distance away from their final position within the core, likely

256   the large glendonite found in the core below (sample U1567C-11X-1; Fig. 3B).

257   *3.2 PXRD*

258   The PXRD analysis of the bulk composition of 5 different glendonites reveal that the glendonites are

259   mostly composed of calcite with a major to minor magnesian calcite component. Minor amounts of

260   quartz, halite, rhodochrosite ($MnCO_3$) and gypsum were also identified (Table 1 and Supplementary

261   Material Fig. S11).

262   *3.3 Microscopy*

263   Polished thin sections were examined by light microscopy and revealed several different carbonate

264   phases (Figs. 4 and 5). These have been grouped by appearance (colour, texture, relationship to other

265   phases) and geochemistry (Table 2). Where possible, these phase names are in keeping with previous

266   studies' description of ikaite carbonate phases (e.g. Huggett et al., 2005; Grasby et al., 2016; Vickers

267   et al., 2018; Mikhailova et al., 2021; Scheller et al., 2021; Schultz et al., 2023; Counts et al., *in review*).,

268   with the main phase type assigned based on colour and sub-types based on microstructure and

269   geochemical data.

270   *3.4 LA ICP-MS*

271   The LA ICP-MS trace element data shows that Mg/Ca ratios are distinct on average between the

272   carbonate phases, with Type 1A ≤ 1B ≤ 2A = 2B ≤ 0, albeit with substantial heterogeneity within a

273   phase such that the ranges overlap in most cases (Fig. 6). There is also substantial overlap between

274   types 1 and 2 for all other measured elemental ratios (Fe/Ca, Mn/Ca, Sr/Ca, P/Ca, S/Ca; Fig. 6). The

275   measurements made from the outer hard crust of the glendonite sample from core U1569A-19R-2

276   show the highest Mg/Ca contents of all, and distinctly higher S/Ca than all other carbonate phases.

277   Type 0 has significantly higher Mn/Ca and P/Ca than all other measured calcite phases, and

278   significantly lower S/Ca than other measured carbonate phases (Fig. 6).

279   *3.5 ICP-OES*

280   Bulk drill-sampled ICP-OES results find that the Exp. 396 glendonites have Mg/Ca ratios in the range

281   of c. 20 - 50 mmol/mol, comparable to the Fur Formation carbonates (Fig 7). Sr/Ca range from 1.5 -

282   1.8 mmol/mol; Fe/Ca from 1.6 - 38 mmol/mol, with an outlier of 165 mmol/mol (1568A 15X 4 55-58);

283   Mn/Ca ratios range from 0.4 - 8.4; P/Ca ratios range from 1.5 - 12.8 mmol/mol; and S/Ca ratios range

284   from 0.8 - 5.5 mmol/mol (Fig. 7).

285   *3.6 Microprobe data, 396 ashes*

286   The Exp. 396 ashes all have a basaltic tholeiitic composition, similar to the Fur positive series ashes

287   (Fig. 8). However, they have relatively high MgO content ranging from 4.3 to 9.6 wt%, which is

288   generally higher than that of the Fur positive series (3.3-7.1 wt%; Larsen et al., 2003; Stokke et al.,

289   2020b).

290   *3.7 PHREEQC modelling*

291   Results from the PHREEQC modelling for the interstitial waters are shown in Fig. 9 and in the

292   supplementary data.

293   **4. Discussion**

294   *Ikaite formation and transformation to glendonite*

295   The general microfabric of the glendonites is similar to that observed in previous work on glendonite

296   and transformed ikaite. Notably, areas of calcite blebs with Type 1A cores with 2A overgrowths are

297   also observed in glendonites from Cretaceous to Recent in age, and in modern transformed ikaites

298   (Huggett et al., 2005; Grasby et al., 2016; Vickers et al., 2018; Mikhailova et al., 2021; Scheller et al.,

299   2021; Schultz et al., 2023). The presence of a hardened carbonate rim is also a common feature of

300   glendonites (Fig. 4) (Grasby et al., 2017; Scheller et al., 2022; Schultz et al., 2023; Counts et al., *in*

301   *review*). However, the green Type 0 calcite identified in this study has not been observed in other

302   glendonite thin sections, and appears to be both visually and chemically distinct from the other calcite

303   phases measured in the Exp. 396 glendonites (Fig. 6).

10

304   Based on the geochemical data, we suggest the following model for the sequential formation of the

305   various calcite phases, as illustrated in Fig. 10:

306   Stage 1: The ikaite grew in the sediments, at or just below the sediment-water interface. The Type 0

307   phase appears to have grown directly onto/against the surface of an ikaite crystal, prior to its

308   decomposition, suggesting it may represent the earliest preserved phase present (Fig. 10).

309   Stage 2: Chemical and thermal conditions changed as burial continued, and the ikaite started to break

310   down (Fig. 10). The formation of 1A blebs began during the recrystallisation reaction, preferentially

311   excluding Mg from the crystal structure, leading to a highly localisedincrease of Mg^{2+} in the pore

312   waters. Where breakdown was rapid, larger areas of Type 1B formed, including more Mg in the

313   structure than 1A due to the rapidity of the reaction. Then, Types 2A and 2B grew, incorporating more

314   Mg into the calcite structure than the Types 1 due to its now higher concentration in the local waters.

315   Stage 3: An undetermined length of time later, after continued burial, Type 3 fibrous syntaxial and/or

316   isopachous sparry calcite forms in some of the pore spaces in the ikaite, growing from the surface of

317   Types 1 and/or 2 calcite phases (Fig. 10). Note that all phases grouped as Types 1 and 2 are believed

318   to have formed directly from ikaite (i.e. the $CaCO_3$ is believed to have been entirely or dominantly

319   sourced directly from the ikaite), whereas we propose that the Type 3 calcite formed from a later

320   diagenetic fluid (e.g. Vickers et al., 2020; Counts et al., *in review*). This is based on microfabric and

321   geochemical (elemental and isotopic) data that suggests a very different source fluid. There is very

322   little Type 3 calcite in the Exp. 396 glendonites; much less than is observed in those of the Fur

323   Formation (Vickers et al., 2020). The variable proportion of Type 3 calcite in glendonite is likely

324   responsible for the observed higher bulk Mg/Ca, Mn/Ca and P/Ca ratios than in transformed modern

325   ikaite (Fig. 7).

326   *Relationship to North Atlantic volcanism and timing of ikaite formation*

327   The glendonites of the Exp. 396 cores are found in latest Paleocene, PETM, and (post-PETM) early

328   Eocene-age sediments, within or just above the intervals containing the most numerous and thickest

329   ash layers (Fig. 2 and 11). The only other reported glendonites from this time interval (Paleocene and

330   early Eocene) are also found in the Nordic Seas region, close to the eruptive sites of the North Atlantic

331   Igneous Province (NAIP). Glendonites have been identified in both Paleocene and Eocene strata in

332   Svalbard (Spielhagen and Tripati, 2009; Cui et al., 2021), and in early Eocene strata in northern

333   Denmark (Huggett et al., 2005; Vickers et al., 2020; Fig. 1). In the Danish Paleogene successions,

334   glendonites are only found within the early Eocene Fur Formation that contains over 140 macroscopic

335 ash layers of dominantly tholeiitic basalt composition (Fig. 11; Stokke et al., 2020b; Vickers et al.,

336 2020). The Fur Formation corresponds to the ash-rich Balder and Tare formations offshore in the

337 North Sea and Norwegian margin, respectively (King, 2016). The close stratigraphic association with

338 ash layers within the Nordic Basins suggests that ash deposition and/or diagenesis may play a critical

339 role in ikaite precipitation, in contrast to ikaites found in most modern settings. In modern marine

340 sedimentary settings, the breakdown of sedimentary C_{org} via sulphate reduction, and/or the anaerobic

341 oxidation of methane (AOM) are thought to play a key role in ikaite precipitation, largely because the

342 low $\delta^{13}C$ values measured in ikaites and glendonites suggest an organic or methanogenic source of

343 carbon (e.g. Rogov et al., 2021 and references therein), and also because these organic matter

344 decomposition processes generate DIC (Whiticar et al. 2022). Yet, for ikaite to be precipitated over

345 the more stable $CaCO_3$ polymorphs, factors inhibiting calcite and promoting ikaite precipitation are

346 also required. These may include high alkalinity, high concentrations of phosphate and/or Mg^{2+}, and

347 low temperatures (Rickaby et al., 2006; Zhou et al., 2015; Purgstaller et al., 2017; Stockmann et al.,

348 2018). Volcanic eruptions and subsequent ash deposition may have played a key role in generating

349 such conditions, via both volcanically-driven, short-term climate cooling (e.g. Robock et al., 2000;

350 Schmidt et al., 2016; Stokke et al., 2020a), and through rapid diagenesis of these ashes generating the

351 chemical conditions in the pore waters that could have promoted ikaite precipitation (e.g. Gislason

352 and Oelkers, 2011; Olsson et al., 2014; Murray et al., 2018). Indeed, ikaite and other carbonates were

353 discovered as travertine in the Hvanná river in the vicinity of the Eyjafjallajökull volcano shortly after

354 eruptive activity began in Spring of 2010 (Olsson et al., 2014).

355 Compositional data from Exp. 396 shows that the ashes, like those from the Fur positive series (Stokke

356 et al., 2020b), are tholeiitic (Fig. 8). Basaltic volcanic material undergoes rapid chemical weathering

357 (e.g. Gislason and Oelkers, 2011), thus we suggest that the chemical alteration of these tholeiitic ashes

358 could have generated the chemical conditions which promoted ikaite formation, which may include

359 increasing alkalinity and [Ca^{2+}], driving changes in aqueous Mg/Ca (e.g. Gislason and Oelkers, 2011;

360 Olsson et al., 2014; Purgstaller et al., 2017; Murray et al., 2018; Tollefsen et al., 2020). Pore waters

361 from recovered cores were taken on-board at low resolution and geochemically analysed (Planke et

362 al., 2023). These measurements reflect the conditions in the core interstitial waters today, some c. 55

363 million years since deposition, and therefore do not reflect conditions immediately prior to ikaite

364 precipitation. Nonetheless, these pore water profiles may provide remnant signatures of post-

365 depositional processes and therefore shed light on how ash diagenesis may have altered local pore

366 water chemistry, promoting ikaite precipitation.

367   The pore water profiles show a strong, sharp change in pH and carbon speciation across the ash-

368   bearing intervals, likely a retained signal of the dissolution/leaching of the ashes themselves (Fig. 11).

369   While pore water chemistry certainly continued to evolve over the last 55 million years, the signature

370   of ash diagenesis on early Paleogene pore waters may have been effectively retained, being buffered

371   against later fluid flow and associated later overprinting reactions by the over- and under-lying clay-

372   rich strata (Planke et al., 2023; Fig. 2). High smectite contents formed from the weathering of silicate

373   material such as basaltic ash both *in situ* and in terrestrial catchment areas, can result in 'aquitard'

374   deposits characterised by very low permeability and low effective porosity (Hendry et al., 2015). This

375   allows large concentration gradients to develop within the sediment pile, as documented along ash-

376   rich margins globally (Torres et al. 1995 and references therein). The major fluctuations in pH,

377   alkalinity, and Ca/Mg ratios across these ash-rich intervals at Modgunn and Mimir (Longman et al., *in*

378   *review*; Planke et al., 2023) suggests that these pore waters are likely to have evolved in semi-isolation

379   from over- and underlying strata. Therefore, if the pore water system is closed, the evolution of the

380   pore water chemistry may be limited. Alternatively, long-term diagenesis of ash minerals may be

381   continually altering pore water chemistry across these intervals with some diffusive exchange across

382   the low-permeability clay boundaries, yet still providing an indication of the degree to which ash

383   alteration may impact fluid composition. Pore water measurements through selected cores show that

384   the glendonite-bearing levels associated with volcanic ash are coincident with relatively elevated pH

385   and lower alkalinity, although alkalinity change across ash-rich intervals is less abrupt (Fig. 11). The

386   carbonate chemistry of these pore waters is controlled by a complex balance between $CaCO_3$

387   dissolution/precipitation, respiration of organic carbon, and at these sites, probably by alkalinity

388   generation from the dissolution of ash (Longman et al. 2021). As such, it is difficult to ascribe the

389   observed pore water carbonate chemistry changes (Fig. 11) to any one process. However, the

390   relatively high pH and low alkalinity relative to the over- and underlying mud-rich sediments is

391   consistent with alkalinity generation via ash dissolution, resulting in increased TAlk and pH, being

392   counteracted by $CaCO_3$ precipitation, drawing down carbonate alkalinity. Our observation of abundant

393   $CaCO_3$ in the form of ikaite and later diagenetic phases in these ash-rich sediments is consistent with

394   this hypothesis. Further, PHREEQC simulations indicate a clear difference in carbonate speciation

395   across ash-rich, glendonite bearing intervals with lower $[CO_2]_{aq}$, and higher $[CO_3^{2-}]$ and $[CaCO_3^0]$ (Fig.

396   9) compared with surrounding intervals. Aragonite and calcite saturation indices go from under- to

397   oversaturated, and dolomite shows enhanced oversaturation, across these intervals (Fig. 9).

398   *Timing and conceptual model for ikaite growth*

399 Zhou et al. (2015) examined modern marine sedimentary ikaite bearing sites and identified "Ikaite

400 Formation Zones" (IFZs) based on where the decreasing $[Ca^{2+}]$ downcore profile intersects the

401 increasing DIC profile (calculated by maximum $[Ca^{2+}]$ x DIC). The IFZ is thus highly variable, as it

402 depends on the amount of organic matter (carbon source) present, which in turn is linked to processes

403 such as sedimentation rate and primary productivity. In modern settings, this is generally between 2

404 – 15 m within the sediment pile (Zhou et al., 2015). In the early Paleogene Norwegian Margin, infill

405 sedimentation rates of hydrothermal vent complex craters were very high. Taking the very

406 conservative estimate of a hydrothermal vent infill duration of 43 kyr for the Modgunn crater (Berndt

407 et al., 2023), the glendonite-bearing horizons for the vent infill cores would have been at depths of

408 below 15 m within 8 kyr for Hole U1568A and 16.5 kyr for Hole U1567C. For sediments such as those

409 encountered in Modgunn and Mimir, the primary driver of DIC and $[Ca^{2+}]$ is believed to be diagenesis

410 of the ashes rather than organic matter (e.g. Gislason and Oelkers, 2011). Given that the diagenesis of

411 fresh volcanic material occurs very rapidly after deposition (on timescales of shorter than a month;

412 Hembury et al., 2012; Olsson et al., 2014), the ikaite formation zones are likely to have been much

413 shallower than 15 m at the time of ikaite precipitation, possibly near the sediment-water interface.

414 Observations on the relationship between the Exp. 396 glendonites and the host sediments support

415 this theory. For example, it can be seen that the pale grey sediment is displaced immediately around

416 the glendonite shown in Fig. 3E, yet an ash layer 2 cm above shows no displacement. In Fig. 3F, the

417 pale grey sediment that the glendonite has grown in is displaced, yet the ash that is deposited on top,

418 two thirds up the height of the glendonite, shows no displacement at the top, suggesting the top of

419 the ikaite crystal was potentially protruding into the water column from the seafloor at the time of

420 the ash fall. Therefore, it can be deduced that these parent ikaites grew in the soft sediment prior to

421 compaction, possibly just centimetres below the sediment-water interface. In the Danish succession,

422 similar "boudinage" textures are observed around both glendonites and tree branch fossils in the Fur

423 Formation (Schultz et al., 2022). This indicates that the ikaites grew at or close to the sediment-water

424 interface, as they exhibit the same relationship to the host sediment as tree branches that came to

425 rest on top of or sticking into the top few centimetres or decimetres of sediment. In case of the Exp.

426 396 glendonites, which occur in rapidly deposited sediments, the parent ikaites must have grown

427 quickly, on timescales of years, for these relationships to be observed. Modern ikaites have been

428 known to grow to cm-scale crystals on timescales of months to years (Boch et al., 2015; Schultz et al.,

429 2022, 2023), suggesting that this is indeed possible. In one case, one month after final construction of

430 a concrete riverbed in Alpine Austria, cm-thick ikaite crystal aggregates were discovered to have

431 formed (Boch et al., 2015); in another instance, ikaite crystals 3 cm long were found growing next to

432   a reservoir causeway in Utqiaġvik, Alaska, some 3 years after its construction (Schultz et al., 2022;

433   2023).

434   Thus, we argue that the parent ikaites to Exp. 396 glendonites grew on geologically synchronous

435   timescales to the sediments in which they are found. Their occurrence and rapid growth during the

436   Paleocene-Eocene greenhouse climate were likely facilitated by the unique conditions near the active

437   NAIP. We propose a scenario in which the chemical environment that stabilised ikaite was provided

438   by the early and rapid diagenesis of the (frequent) ashes deposited from the NAIP. At the same time,

439   volcanism may have also may also have played a critical role in driving short-term (c. sub-decadal

440   scale) cooling which additionally helped promote the formation of ikaite.

441   Paleotemperature estimates from carbonate clumped isotope thermometry of the glendonites from

442   northern Denmark, and via sedimentary lipid biomarkers, show intervals of cooling which are

443   apparently at odds with global records (e.g. Frieling et al., 2014; Evans et al., 2018; Sluijs et al., 2020;

444   Westerhold et al., 2020; Meckler et al., 2022). Specifically, clumped isotope temperatures from the

445   early Eocene Danish glendonites have been interpreted as recording cold bottom water temperatures

446   for this < 200 m deep basin (1 ± 5 and 9 ± 4 °C; Vickers et al., 2020), and sharp, short-lasting cooling

447   was found in reconstructed near-surface temperatures (reconstructed using lipid biomarker proxies)

448   in the Paleocene-Eocene of the Danish succession (near-surface temperatures dropped below 15 °C;

449   summarised in Jones et al., 2023). This has led to speculation that short, sharp, transient cooling

450   events occurred, possibly only on a regional scale, or most pronounced, in the Nordic Seas (Stokke et

451   al., 2020a; Vickers et al., 2020). Evidence for sudden/short duration cooling is absent from some

452   nearby sites from similar time periods (e.g. Belgian/Paris basin, Evans et al., 2018; West Siberian Sea

453   and the Arctic, Frieling et al., 2014 and references therein), all of which were characterised by SST of

454   ~20-30°C during this time. This further highlights that the very cool temperatures indicated by the

455   presence of glendonites in this region must presumably be a localised or extremely transient

456   phenomenon. Such regional cooling episodes may result from, for example, a series of short-lived

457   volcanic 'winters' caused by sulphur degassing during effusive and explosive eruptions (Robock et al.,

458   2000; Schmidt et al., 2016; Stokke et al., 2020a). Given the sub-decadal residence time of sulphur in

459   the atmosphere, this climate forcing would require many closely-spaced eruptions to maintain its

460   cooling effect on timescales of centuries to millennia (Jones et al., 2016). However, since ikaite appears

461   to have grown very rapidly in some of the successions in the Nordic Seas, a growth rate of this

462   magnitude does not seem implausible.

463 In addition to possible volcanically-driven regional climatic events, the unique paleogeography of the

464 region were likely critical for providing the conditions required for ikaite formation. The Nordic Seas

465 were a series of hydrographically and/or geographically semi-restricted, relatively shallow basins with

466 varying connectivity to the Atlantic, Tethys, and Arctic oceans across the Paleocene–Eocene interval

467 (Fig. 1), with several lines of evidence suggesting that maximum restriction occurred in the post-PETM

468 early Eocene (Zacke et al., 2009; Hovikoski et al., 2021; Jones et al., 2023). Such restricted conditions

469 could imply bottom waters in individual basins (simultaneously or at different times) may have been

470 effectively isolated from the global ocean. Without sufficient exchange with the global ocean, bottom

471 waters colder than the global deep ocean, that may have formed during transient cool conditions such

472 as volcanic winters, could have led to the formation of a cold bottom layer in a heavily stratified water

473 column in the Nordic Sea basins for a prolonged period. Finally, the thermal uplift and emplacement

474 of a continental flood basalt province created an extensive high-altitude plateau to the west of the

475 shallow seaways that marked the region, which is likely to have altered the positioning, oscillation,

476 and intensity of the Paleogene northern hemisphere jet stream (Jones et al., 2023). While no studies

477 have investigated this potential effect, it is reasonable to assume that a regional microclimate was

478 likely present in the Nordic Seas at this time. It is possible that a combination of factors led to a bias

479 towards the recording of winter temperatures in the bottom waters of the basin (Vickers et al., 2020).

480 If a long, severe cooling forcing such as a sustained volcanic winter occurred, cooling of the surface

481 waters could eventually have triggered a dense water cascade, bringing these cold, dense waters to

482 the bottom of the basin system. Being restricted and stratified, these cold waters could potentially

483 have remained at the bottom of the basin system for a long time (years) (e.g. Vickers et al., 2020) such

484 that, together with ample volcanic ash supply, it seems plausible that the local conditions coincided

485 to create the necessary conditions for ikaite growth in a hothouse climate.

486 **5. Conclusions**

487 Glendonites are found throughout the Late Paleocene and early Eocene sediments from the IODP Exp.

488 396 cores, including those deposited during the PETM, and closely associated with the volcanic ashes

489 from the nearby NAIP. High-resolution examination and sedimentary logging of these cores reveals

490 ten glendonite horizons, six in the post-PETM sections recovered from the Mimir transect, three from

491 the PETM interval of the hydrothermal vent infill collected in the Modgunn Transect, and one from

492 the pre-PETM interval of this hydrothermal vent infill. Observations of their relationship to their host

493 sediments suggest they grew within centimetres of the sediment-water interface, sometimes even

494 protruding into the water column. Based on known time-scales of ash diagenesis and ikaite growth,

495 we argue that the parent ikaites grew rapidly, within timescales of years to decades after ash

496   deposition. Examination of thin-sections of the glendonites via a number of geochemical methods

497   reveals that the Exp. 396 glendonites show a range of carbonate phases, including fabrics not

498   previously observed in other glendonites nor transformed natural ikaite. These features suggest that

499   their parent ikaite growth environment was unusual even for ikaite, and the leaching and rapid early

500   diagenesis of the NAIP volcanic ashes likely generated the required pore water conditions that

501   stabilised ikaite over other calcium carbonate polymorphs. Paleothermometry studies for the Nordic

502   Seas Region during this time suggest that seawater temperatures were punctuated by remarkably

503   cold, short-term events, although no such temperature deviations have been found outside of this

504   region. Glendonites are also found in the Paleocene and Eocene succession of Svalbard, and in the

505   early Eocene (post-PETM) succession of Denmark, but nowhere outside of this semi-enclosed shallow

506   basin.

507   The close association of glendonites to ash in the Exp. 396 succession, and likewise in the early Eocene

508   of Denmark, along with biomarker and clumped isotope thermometry evidence of episodic transient

509   cooling events, supports our theory that the eruptive phases of the NAIP led to ikaite precipitation in

510   the Nordic Seas region. This was both a chemical and thermal effect: the early diagenesis of the ashes

511   likely drove pore water conditions chemically favourable to ikaite, and the eruptions could have

512   caused transient volcanic winters that were much colder than the prevailing background climate of

513   the time. The unique paleogeography of the region may have led to the basin bottom waters being

514   biased towards these anomalously cold temperatures for years or even decades, allowing the ikaites

515   to grow to the centimetre to >decimetre sizes we observe. Further work is required to test this

516   hypothesis, including detailed, high resolution multi-proxy temperature reconstructions e.g. via

517   clumped isotope thermometry of the glendonites themselves, and biomarker and palynological

518   assemblage-based temperature reconstructions for the sediments of these cores.

519   **Figures and Tables**

520   **Figure 1: (A)** Paleogeographic map of the Nordic Seas region with North Atlantic Igneous Province

521   volcanism shown, after Jones et al. (2023). Location of all known Paleocene – Eocene glendonite

522   bearing sites marked – Exp. 396 Modgunn and Mimir cores (this study); Paleogene-Eocene sediments

523   of Svalbard (Spielhagen and Tripati, 2009), and early Eocene Fur Formation of northern Denmark

524   (Vickers et al., 2020). **(B)** High-resolution 3-D seismic data for holes 1568 and 1567 along the Modgunn

525   transect (from Planke et al., 2023). **(C)** High-resolution 3-D seismic data for holes 1569 and 1570 along

526   the Mimir Transect (from Planke et al., 2023). Holes from which glendonites were recovered are

527   shown in red. PETM intervals are shown in yellow.

528   **Figure 2:** Overview logs of the cores with glendonite horizons marked by the red glendonite cartoon.

529   (A) The Mimir (U1569 - U1570) transect, from Planke et al. (2023). For the correlations between cores,

530   all ties (solid black lines) are supported by lithologic change and biostratigraphic zonation. The dashed

531   line represents correlation by lithologic change within a biostratigraphic zone, aiming to tie Hole

532   U1570C to Hole U1570D (Planke et al., 2023). (B) The Modgunn (U1567 - U1568) transect, from Planke

533   et al. (2023). Core sections of PETM age are highlighted in yellow, and the hydrothermal vent infill

534   (e.g. Fig. 1B) is shown in grey. All correlations between cores are supported by lithologic change,

535   biostratigraphic zonation, and carbon isotope stratigraphy (Berndt et al., 2023).

536   **Figure 3:** Photographs of glendonites *in situ* in the cores from the Modgunn and Mimir transects. **(A)**

537   Glendonite fragments in drill mud from 1567C-10X-3 40-45 (MLV 86). **(B)** Glendonite from section

538   1567C-11X-1 94-95 (MLV 57, 97). **(C)** Cemented glendonite from section 1569A-19R-2 54-62 (MLV 90).

539   **(D)** Glendonite from section 1570A-15R-1 108-112 (MLV 92). **(E)** Glendonite fragment in 1570A-15R-1

540   22-25 (MLV 91). **(F)** Glendonite from section 1570A-25R-1 (MLV 93).

541   **Figure 4:** Photomicrographs of polished thin sections from selected Exp. 396 glendonites. The blue

542   background colour is derived from the resin rather than the glendonite. **(A)** and **(B)** show the typical

543   harder outer rim with more porous centre characteristic of transformed ikaite (e.g. Schultz et al.,

544   2023). Red dots labelled 8, 9 and 10 are spots where LA ICP-MS analysis was performed. The

545   glendonites commonly show areas of different calcite types defined by colour, which are often hard

546   to place into the "traditional" carbonate phase types seen in other glendonites (e.g. Huggett et al.,

547   2005; Vickers et al., 2018). **(C)** shows a distinct boundary between white Type 2B calcite and brown

548   Type 1B calcite, neither of which show zoning defined by colour or porosity. **(D)** shows the sharp

549   boundary between green Type 0 carbonate, with black dendritic surface growth, and other calcite

550   phases. The shape of the sharp boundary that Type 0 defines on one side suggests that Type 0 grew

551   on the surface of and out from an ikaite crystal, which later broke down to leave void space and

552   patches of Type 1B with 2B overgrowths. **(E)** and **(F)** show patches of more typical zoned calcite blebs,

553   here labelled 1A and 2A, which appear to fit into the traditional categories of "Type I" (zoned brown

554   calcite forming the centre of the blebs) and "Type II" (zoned pale overgrowths on Type I; e.g. Vickers

555   et al., 2018; Schultz et al., 2023). **(G)** Apparent reversal of the "typical" glendonite fabric, whereby the

556   central area of the calcite blebs is pale/white Type 2B and the overgrowth brown Type 1B calcite. This

557   contrasts with **(H)** which shows dark Type 1A with white Type 2A overgrowths.

558   **Figure 5:** Light microscopy, SEM photomicrographs and EDS element maps from thin sections of

559   glendonites at 1569A-19R-2 and 1567C-11X-1. **(A)** Overview under plane polarised light of the area

560   examined for glendonite at 1569A-19R-2, with the carbonate phases labelled. **(B)** BSE image of the

561   same area. Higher porosity in the Type 1 can be seen. **(C)** BSE image of zoomed in area of Type 2B with

562   Type 1B overgrowth. Higher porosity of Type 1 is again clear. **(D)** EDS map showing Mg distribution

563   across calcite types 1B and 2B, overlaid on the BSE photomicrograph. **(E)** The same map without the

564   BSE photomicrograph **(F)** EDS map showing Mg distribution across calcite types 1A, 2A and 2B. **(G)**

565   Overview under plane polarised light of the area examined for glendonite at 1567C-11X-1. **(H)** BSE

566   image of the same area, with pop-out **(I)** showing the microcrystalline nature of Type 0. **(J)**

567   Magnification of the same area with types IB and 2B calcite under BSE. **(K)** EDS element map showing

568   the Mg distribution across the same area.

569   **Figure 6:** LA ICP-MS element/Ca data for points across the Exp. 396 glendonite polished thin sections.

570   The data have been grouped according to the calcite types described in the main text and in the

571   preceding figures. Photomicrograph showing the location points 8 – 11 from outer edge inwards are

572   shown bottom right, and also in Fig. 4A. Photomicrographs showing the location of all the individual

573   points measured may be found in the Supplementary Material.

574   **Figure 7:** Element/Ca ratios of the Exp. 396 glendonites and associated calcites compared to published

575   ICP-OES data for other glendonite-bearing sites.

576   **Figure 8: (A)** A Total Alkali Silica (TAS) plot comparing the Exp. 396 ashes (this study) to published data

577   for both positive (Stokke et al. 2020b) and negative (Larsen et al., 2003) ash series of the Fur Formation

578   in northern Denmark. The Exp. 396 ashes and Fur positive series fall into the basaltic fields, whereas

579   the Fur negative series show much more variation and have overall more felsic compositions. Note

580   that while the Fur positive series data are microprobe analyses of matrix glass, the Fur Negative series

581   data are whole rock data. However, the whole rock samples were leached of clay prior to analysis and

582   no significant dilution is expected. **(B)** Ternary Alkali-Iron-Magnesium (AFM) diagram showing that the

583   basaltic ashes from both the Exp. 396 sites and the Fur positive series are tholeiitic basalts. Note that

584   many of the Exp. 396 ashes have higher MgO content than the Fur positive ashes.

585   **Figure 9:** PHREEQC simulation results for the U1568A core, which spans the hydrothermal vent infill

586   (grey highlight labelled 'HTV'). Note that HCO_3^- (the major species) is not shown.

587   **Figure 10:** Schematic of ikaite transformation in the Exp. 396 cores, adapted from Counts et al. (*in*

588   *review*) based on observed textural relationships and geochemistry of the calcite phases in the Exp.

589   396 glendonites.

590 **Figure 11: (A)** Relative position of glendonites in the Paleocene-Eocene sediments of selected cores

591 from the mid-Norwegian Margin, Exp. 396, compared to measured ash thicknesses. Pore water

592 alkalinity and pH data (Planke et al., 2023) are also shown. Pale grey indicates the PETM-aged intervals

593 in the stratigraphy. Note that for U1569A, core recovery was poor, particularly in the bottom, ash-

594 bearing part (see Fig. 2). High ash contents lead to lower core recovery as they are course-grained and

595 unlithified; therefore it is likely that there were much more numerous and thicker ash horizons in the

596 interval between 18R and 37R (c. 180 – 340 mbsf). (B) Relative position of glendonites in the

597 Paleocene-Eocene sediments of Northern Denmark, compared to ash thicknesses per metre (Jones et

598 al., 2023). Glendonite horizons for the Fur Formation are from Vickers et al., (2020) (solid lines) and

599 dashed line as identified by Henrik Friis, pers. comm. Pale grey indicates the end of the body of the

600 PETM carbon isotope excursion (Jones et al., 2023). The recovery phase is between ashes -33 and -

601 21a. SC = Stolleklint Clay.

602 **Table 1:** Glendonites of the Exp. 396 cores, PXRD data from bulk glendonite analysis, element/Ca

603 ratios.

604 **Table 2:** Descriptions of the different carbonate phases observed within the glendonites through thin

605 section microscopic and geochemical analysis (light microscopy, SEM, EDS and LA-ICP-MS).

606 **Team List**

607 The IODP expedition 396 Scientists are: S. Planke, C. Berndt, C.A. Alvarez Zarikian, A. Agarwal, G.D.M.

608 Andrews, P. Betlem, J. Bhattacharya, H. Brinkhuis, S. Chatterjee, M. Christopoulou, V.J. Clementi, E.C.

609 Ferré, I.Y. Filina, J. Frieling, P. Guo, D.T. Harper, M.T. Jones, S. Lambart, J. Longman, J.M. Millett, G.

610 Mohn, R. Nakaoka, R.P. Scherer, C. Tegner, N. Varela, M. Wang, W. Xu, and S.L. Yager

611 **Author contribution**

612 MLV designed the study, undertook sampling and high-resolution logging, photographed and

613 examined thin-sections under a light microscope and SEM, co-ran LA-ICPMS analysis, lead the writing

614 of the manuscript.

615 MTJ undertook PHREEQC modelling, assisted in the interpretation of the data and co-wrote the

616 manuscript.

617 JL undertook the ash thickness measurements, assisted in the interpretation of the data, co-wrote the

618 manuscript and assisted with the logging and sampling.

619   DE ran the LA-ICPMS and assisted in the interpretation of the data and writing of the manuscript.

620   CVU undertook the ICP-OES analysis.

621   ES carried out microprobe analysis of the ashes and plotting of this data.

622   MV undertook the PXRD analysis.

623   JF assisted in the interpretation of the data and co-wrote the manuscript.

624   DTH assisted in the interpretation of the data and co-wrote the manuscript.

625   VJC assisted in the interpretation of the pore-water data and co-wrote the manuscript.

626   IODP E396 S: undertook drilling of the cores, all shipboard analysis, and sampling.

627   **Competing interests**

628   The authors declare that they have no conflict of interest.

642   **References**

643   Alley, N.F., Hore, S.B. and Frakes, L.A.. Glaciations at high-latitude Southern Australia during the Early

644   Cretaceous. Aust. J. Earth Sci., 67(8), 1045-1095, https://doi.org/10.1080/08120099.2019.1590457,

645   2020

646   Berndt, C., Planke, S., Alvestad, E., Tsikalas, F., and Rasmussen, T. Seismic volcanostratigraphy of the

647   Norwegian Margin: constraints on tectonomagmatic break-up processes. J. Geol. Soc. London, 158(3),

648   413–426. https://doi.org/10.1144/jgs.158.3.413, 2001.

649   Berndt., C., Planke, S., Alvarez Zarikian, C.A., Frieling, J., Jones, M.T., Millett, J.M., Brinkhuis, H., Bünz,

650   S., Svensen, H.S., Longman, J., Scherer, R.P., Karstens, J., Manton, B., Nelissen, M., Reed, B., Faleide,

651   J.I., Huismans, R.S., Agarwal, A., Andrews, G.D.M., Betlem, P., Bhattacharya, J., Chatterjee, S.,

652   Christopoulou, M., Clementi, V.J., Ferré, E.C., Filina, I.Y., Guo, P., Harper, D.T., Lambart, S., Mohn, G.,

653   Nakaoka, R., Tegner, C., Varela, N., Wang, M., Xu, W., Yager, S.L. (2023). Shallow-water hydrothermal

654   venting linked to the Paleocene Eocene Thermal Maximum. Nat. Geosci., *in press.*

655   Boch, R., Dietzel, M., Reichl, P., Leis, A., Baldermann, A., Mittermayr, F. and Pölt, P.. Rapid ikaite

656   ($CaCO_3 \cdot 6H_2O$) crystallization in a man-made river bed: hydrogeochemical monitoring of a rarely

657   documented   mineral   formation.   Appl.   Geochem.,   63,   366-379,

658   https://doi.org/10.1016/j.apgeochem.2015.10.003 , 2015.

659   Buchardt, B., Israelson, C., Seaman, P. and Stockmann, G. Ikaite tufa towers in Ikka Fjord, southwest

660   Greenland: their formation by mixing of seawater and alkaline spring water. J. Sediment. Res., 71(1),

661   176-189. https://doi.org/10.1306/042800710176, 2001.

662   Council, T.C. and Bennett, P.C. Geochemistry of ikaite formation at Mono Lake, California: implications

663   for   the   origin   of   tufa   mounds.   Geology,   21(11),   971-974.   https://doi.org/10.1130/0091-

664   7613(1993)021<0971:GOIFAM>2.3.CO;2, 1993.

665   Counts, J.W., Vickers, M.L., Stokes, R., Gardner., K., Spivey, W., McAleer, R., Jubb, A., Self-Trail, J.,

666   Gooley, J.T., Lease, R.O., Houseknecht, D.W. Insights into glendonite formation from the Neogene

667   Sagavanirktok Formation, North Slope, Alaska. *(in review for J. of Sediment. Res)*

668   Dieckmann, G.S., Nehrke, G., Papadimitriou, S., Göttlicher, J., Steininger, R., Kennedy, H., Wolf-

669   Gladrow, D. and Thomas, D.N. Calcium carbonate as ikaite crystals in Antarctic sea ice. Geophys. Res.

670   Lett., 35(8). https://doi.org/10.1029/2008GL033540, 2008.

671   Durrant, S.F. Feasibility of improvement in analytical performance in laser ablation inductively coupled

672   plasma-mass spectrometry (LA-ICP-MS) by addition of nitrogen to the argon plasma. Fresenius. J. Anal.

673   Chem+. 349, 768–771. https://doi.org/10.1007/BF00325655, 1994.

674   Evans, D., Müller, W. Automated Extraction of a Five-Year LA-ICP-MS Trace Element Data Set of Ten

675   Common Glass and Carbonate Reference Materials: Long-Term Data Quality, Optimisation and Laser

676   Cell Homogeneity. Geostand. Geoanal. Res. 42, 159–188. https://doi.org/10.1111/ggr.12204, 2018.

677   Evans, D., Sagoo, N., Renema, W., Cotton, L.J., Müller, W., Todd, J.A., Saraswati, P.K., Stassen, P.,

678   Ziegler, M., Pearson, P.N. and Valdes, P.J. Eocene greenhouse climate revealed by coupled clumped

679   isotope-Mg/Ca   thermometry.   P.   Natl.   Acad.   Sci.   USA,   115(6),   1174-1179.

680   https://doi.org/10.1073/pnas.1714744115, 2018.

681   Frieling, J., Iakovleva, A.I., Reichart, G.J., Aleksandrova, G.N., Gnibidenko, Z.N., Schouten, S. and Sluijs,

682   A. Paleocene–Eocene warming and biotic response in the epicontinental West Siberian Sea. Geology,

683   42(9), 767-770. https://doi.org/10.1130/G35724.1, 2014.

684   Garbe-Schönberg, D., Müller, S., 2014. Nano-particulate pressed powder tablets for LA-ICP-MS. J. Anal.

685   At. Spectrom. 29, 990–1000. https://doi.org/10.1039/C4JA00007B, 2014.

686   Gates-Rector, S. and Blanton, T. The powder diffraction file: a quality materials characterization

687   database. Powder Diffr., 34(4), 352-360. https://doi.org/10.1017/S0885715619000812, 2019.

688   Gislason, S.R. and Oelkers, E.H., Chapter 5: Silicate rock weathering and the global carbon cycle.

689   Frontiers in Geochemistry: Contribution of Geochemistry to the Study of the Earth, Harmon, R.S. and

690   Parker, A (eds.), Blackwell Publishing Ltd. 84-103. https://doi.org/10.1002/9781444329957.ch5, 2011.

691   Grasby, S.E., McCune, G.E., Beauchamp, B. and Galloway, J.M., 2017. Lower Cretaceous cold snaps led

692   to widespread glendonite occurrences in the Sverdrup Basin, Canadian High Arctic. Geol. Soc. Am.

693   Bull., 129(7-8), 771-787. https://doi.org/10.1130/B31600.1, 2017.

694   Heinrich, C.A., Pettke, T., Halter, W.E., Aigner-Torres, M., Audétat, A., Günther, D., Hattendorf, B.,

695   Bleiner, D., Guillong, M., Horn, I. Quantitative multi-element analysis of minerals, fluid and melt

696   inclusions by laser-ablation inductively-coupled-plasma mass-spectrometry. Geochim. Cosmochim.

697   Ac. 67, 3473–3497. https://doi.org/10.1016/S0016-7037(03)00084-X, 2003.

698   Hembury, D.J., Palmer, M.R., Fones, G.R., Mills, R.A., Marsh, R. and Jones, M.T. Uptake of dissolved
699   oxygen during marine diagenesis of fresh volcanic material. Geochim. Cosmochim. Ac., 84, pp.353-
700   368. https://doi.org/10.1016/j.gca.2012.01.017, 2012.

701   Hendry, M. J., Solomon, D. K., Person, M., Wassenaar, L. I., Gardner, W. P., Clark, I. D., Mayer, K. U.,
702   Kunimaru, T., Nakata, K., Hasegawa, T. Can argillaceous formations isolate nuclear waste? Insights
703   from   isotopic,   noble   gas,   and   geochemical   profiles,   Geofluids,   15,   381–386,
704   https://doi.org/10.1111/GFL.12132, 2015.

705   Hovikoski, J., Fyhn, M.B.W., Nøhr-Hansen, H., Hopper, J.R., Andrews, S., Barham, M., Nielsen, L.H.,
706   Bjerager, M., Bojesen-Koefoed, J., Lode, S., Sheldon, E., Uchman, A., Skorstengaard, P.R., Alsen, P.
707   Paleocene-Eocene volcanic segmentation of the Norwegian-Greenland seaway reorganized high-
708   latitude   ocean   circulation.   Communications   Earth   &   Environment,   2,   172.
709   https://doi.org/10.1038/s43247-021-00249-w, 2021.

710   Huggett, J.M., Schultz, B.P., Shearman, D.J. and Smith, A.J. The petrology of ikaite pseudomorphs and
711   their   diagenesis.   P.   Geologist.   Assoc.,   116(3-4),   207-220.   https://doi.org/10.1016/S0016-
712   7878(05)80042-2, 2005.

713   Jochum, K.P., Garbe-Schönberg, D., Veter, M., Stoll, B., Weis, U., Weber, M., Lugli, F., Jentzen, A.,
714   Schiebel, R., Wassenburg, J.A., Jacob, D.E., Haug, G.H., 2019. Nano-Powdered Calcium Carbonate
715   Reference Materials: Significant Progress for Microanalysis? Geostand. Geoanal. Res. 43, 595–609.
716   https://doi.org/10.1111/ggr.12292, 2019.

717   Jochum, K.P., Weis, U., Stoll, B., Kuzmin, D., Yang, Q., Raczek, I., Jacob, D.E., Stracke, A., Birbaum, K.,
718   Frick, D.A., Günther, D., Enzweiler, J., 2011. Determination of Reference Values for NIST SRM 610–617
719   Glasses   Following   ISO   Guidelines.   Geostand.   Geoanal.   Res.   35,   397–429.
720   https://doi.org/10.1111/j.1751-908X.2011.00120.x, 2011.

721   Jones, M.T. and Gislason, S.R., 2008. Rapid releases of metal salts and nutrients following the
722   deposition of volcanic ash into aqueous environments. Geochim. Cosmochim. Ac., 72(15), 3661-3680.
723   https://doi.org/10.1016/j.gca.2008.05.030, 2008.

724   Jones, M.T., Jerram, D.A., Svensen, H.H., Grove, C. The effects of large igneous provinces on the global
725   carbon   and   sulphur   cycles.   Palaeogeogr.   Palaeocl.,   441,   4-21.
726   https://doi.org/10.1016/j.palaeo.2015.06.042, 2016.

727   Jones, M.T., Pearce, C.R., Jeandel, C., Gislason, S.R., Eiriksdottir, E.S., Mavromatis, V. and Oelkers, E.H.,

728   2012. Riverine particulate material dissolution as a significant flux of strontium to the oceans. Earth

729   Planet. Sc. Lett., 355, 51-59. https://doi.org/10.1016/j.epsl.2012.08.040, 2012.

730   Jones, M.T., Stokke, E.W., Rooney, A.D., Frieling, J., Pogge von Strandmann, P.A., Wilson, D.J., Svensen,

731   H.H., Planke, S., Adatte, T., Thibault, N.R. and Vickers, M.L. Tracing North Atlantic volcanism and

732   seaway connectivity across the Paleocene–Eocene Thermal Maximum (PETM). Clim. Past, 1-53.

733   https://doi.org/10.5194/egusphere-2023-36, 2023.

734   Kemper, E. (1987). Das Klima der Kreide-Zeit. Geologisches Jeahrbuch, Hannover, reihe A, 96, 5 – 185.

735   King, C., 2016. A Revised Correlation of Tertiary Rocks in the British Isles and Adjacent Areas of NW

736   Europe. Ed. Gale, A.S. and Barry, T.L. Geol. Soc. London, Special Report No. 27.

737   Larsen, L.M., Fitton, J.G. and Pedersen, A.K., 2003. Paleogene volcanic ash layers in the Danish Basin:

738   compositions and source areas in the North Atlantic Igneous Province. Lithos, 71(1), 47-80.

739   https://doi.org/10.1016/j.lithos.2003.07.001, 2003.

740   Longman, J., Palmer, M.R., Gernon, T.M. and Manners, H.R. The role of tephra in enhancing organic

741   carbon preservation in marine sediments. Earth-Sci. Rev, 192, 480-490.

742   https://doi.org/10.1016/j.earscirev.2019.03.018, 2019.

743   Longman, J., Gernon, T.M., Palmer, M.R., Jones, M.T., Stokke, E.W. and Svensen, H.H. Marine

744   diagenesis of tephra aided the Palaeocene-Eocene Thermal Maximum termination. Earth Planet. Sc.

745   Lett., 571, 117101. https://doi.org/10.1016/j.epsl.2021.117101, 2021.

746   Longman, J., Palmer, M.R., Gernon, T.M., Manners, H.R. and Jones, M.T. Subaerial volcanism is a

747   potentially major contributor to oceanic iron and manganese cycles. Communications Earth &

748   Environment, 3(1), 60. https://doi.org/10.1038/s43247-022-00389-7, 2022.

749   Longman, J., Clementi, V.J., Frieling, J., Jones, M.Y., Chatterjee, S., Planke, S., Berndt, C., Alvarez

750   Zarikian, C.A., Betlem, P., Brinkhuis, H., Christopoulou, M., Filina, I.Y., Harper, D.T., Lambart, S., Millett,

751   J.M., Mohn, G.T.F., Scherer, R.P., Varela, N., Xu, W., Yager, S.L., and the IODP Expedition 396 Scientific

752   Party, *in review*. The impact of marine silicate diagenesis in the Norwegian Sea on Early Eocene

753   climate.

754 Meckler, A.N., Sexton, P.F., Piasecki, A.M., Leutert, T.J., Marquardt, J., Ziegler, M., Agterhuis, T.,
755 Lourens, L.J., Rae, J.W.B., Barnet, J., Tripati, A., and Bernasconi, S.M. Cenozoic evolution of deep ocean
756 temperature from clumped isotope thermometry. Science, 377(6601), 86-90.
757 https://doi.org/10.1126/science.abk0604, 2022.

758 Merkel, A. and Munnecke, A., 2023. Glendonite-bearing concretions from the upper Pliensbachian
759 (Lower Jurassic) of South Germany: indicators for a massive cooling in the European epicontinental
760 sea. Facies, 69(3), 10. https://doi.org/10.1007/s10347-023-00667-6 , 2023.

761 Mikhailova, K.Y., Rogov, M.A., Ershova, V.B., Vasileva, K.Y., Pokrovsky, B.G. and Baraboshkin, E.Y. New
762 data on stratigraphy and distributions of glendonites from the carolinefjellet formation (Middle
763 Aptian–Lower Albian, Cretaceous), Western Spitsbergen. Stratigr. Geo. Correl+, 29, 21-35.
764 https://doi.org/10.1134/S0869593821010056, 2021.

765 Murphy, B.H., Farley, K.A. and Zachos, J.C. An extraterrestrial 3He-based timescale for the Paleocene–
766 Eocene thermal maximum (PETM) from Walvis Ridge, IODP Site 1266. Geochim. Cosmochim. Ac.,
767 74(17), pp.5098-5108. https://doi.org/10.1016/j.gca.2010.03.039, 2010.

768 Olsson, J., Stipp, S.L.S., Dalby, K.N. and Gislason, S.R. Rapid release of metal salts and nutrients from
769 the 2011 Grímsvötn, Iceland volcanic ash. Geochim. Cosmochim. Ac., 123, pp.134-149.
770 https://doi.org/10.1016/j.gca.2013.09.009, 2013.

771 Olsson, J., Stipp, S.L.S., Makovicky, E. and Gislason, S.R. Metal scavenging by calcium carbonate at the
772 Eyjafjallajökull volcano: A carbon capture and storage analogue. Chem. Geol., 384, 135-148.
773 https://doi.org/10.1016/j.chemgeo.2014.06.025, 2014.

774 Parkhurst, D.L., and Appelo, C.A.J. Description of input and examples for PHREEQC version 3—A
775 computer program for speciation, batch-reaction, one-dimensional transport, and inverse
776 geochemical calculations: U.S. Geological Survey Techniques and Methods, book 6, chap. A43, 497,
777 https://doi.org/10.3133/tm6A43, 2013.

778 Pearce, N.J.G., Perkins, W.T., Westgate, J.A., Gorton, M.P., Jackson, S.E., Neal, C.R., Chenery, S.P. A
779 Compilation of New and Published Major and Trace Element Data for NIST SRM 610 and NIST SRM 612
780 Glass Reference Materials. Geostandard. Newslett. 21, 115–144. https://doi.org/10.1111/j.1751-
781 908X.1997.tb00538.x, 1997.

782   Planke, S., Berndt, C. and Alvarez Zarikian, C.A. Mid-Norwegian Margin Magmatism and Paleoclimate

783   Implications-Expedition 396 of the R/V JOIDES Resolution from and to Reykjavík, Iceland, Sites U1565–

784   U1574, 6 August–5 October 2021. Proceedings of the International Ocean Discovery Program, 396.

785   https://doi.org/10.14379/iodp.proc.396.2023, 2023.

786   Purgstaller, B., Dietzel, M., Baldermann, A. and Mavromatis, V. Control of temperature and aqueous

787   Mg2+/Ca2+ ratio on the (trans-) formation of ikaite. Geochim. Cosmochim. Ac., 217, 128-143.

788   https://doi.org/10.1016/j.gca.2017.08.016, 2017.

789   Rickaby, R., Shaw, S., Bennitt, G., Kennedy, H., Zabel, M. and Lennie, A. Potential of ikaite to record

790   the evolution of oceanic δ18O. Geology, 34(6), 497-500. https://doi.org/10.1130/G22413.1, 2006.

791   Robock,   A.   Volcanic   eruptions   and   climate.   Rev.   Geophys.,   38(2),   191-219.

792   https://doi.org/10.1029/1998RG000054, 2000.

793   Rogov, M.A., Ershova, V.B., Shchepetova, E.V., Zakharov, V.A., Pokrovsky, B.G., and Khudoley, A.K.

794   Earliest Cretaceous (late Berriasian) glendonites from Northeast Siberia revise the timing of initiation

795   of transient Early Cretaceous cooling in the high latitudes: Cretaceous Res., 71, 102–112.

796   https://doi.org/10.1016/j.cretres.2016.11.011, 2017.

797   Rogov, M., Ershova, V., Vereshchagin, O., Vasileva, K., Mikhailova, K. and Krylov, A. Database of global

798   glendonite and ikaite records throughout the Phanerozoic. Earth Syst. Sci. Data, 13(2), 343-356.

799   https://doi.org/10.5194/essd-13-343-2021, 2021.

800   Rogov, M., Ershova, V., Gaina, C., Vereshchagin, O., Vasileva, K., Mikhailova, K. and Krylov, A.

801   Glendonites   throughout   the   Phanerozoic.   Earth-Sci.   Rev.,   104430.

802   https://doi.org/10.1016/j.earscirev.2023.104430, 2023.

803   Röhl, U., Westerhold, T., Bralower, T.J. and Zachos, J.C. On the duration of the Paleocene-Eocene

804   thermal   maximum   (PETM).   Geochemistry,   Geophysics,   Geosystems,   8(12).

805   https://doi.org/10.1029/2007GC001784, 2007.

806   Scheller, E.L., Grotzinger, J. and Ingalls, M. Guttulatic calcite: A carbonate microtexture that reveals

807   frigid formation conditions. Geology, 50(1), 48-53. https://doi.org/10.1130/G49312.1, 2022.

808   Schmidt, A., Skeffington, R.A., Thordarson, T., Self, S., Forster, P.M., Rap, A., Ridgwell, A., Fowler, D.,

809   Wilson, M., Mann, G.W. and Wignall, P.B. Selective environmental stress from sulphur emitted by

810   continental flood basalt eruptions. Nat. Geosci., 9(1), 77-82. https://doi.org/10.1038/ngeo2588, 2016.

811   Schoon, P.L., Heilmann-Clausen, C., Schultz, B.P., Damasté, J.S.S., Schouten, S. Warming and

812   environmental changes in the eastern North Sea Basin during the Palaeocene–Eocene Thermal

813   Maximum   as   revealed   by   biomarker   lipids.   Org.   Geochem.   78,   79-88.

814   https://doi.org/10.1016/j.orggeochem.2014.11.003, 2015.

815   Schultz, B., Thibault, N. and Huggett, J. The minerals ikaite and its pseudomorph glendonite: Historical

816   perspective and legacies of Douglas Shearman and Alec K. Smith. P. Geologist. Assoc., 133(2), 176-192.

817   https://doi.org/10.1016/j.pgeola.2022.02.003, 2022.

818   Schultz, B.P., Huggett, J.M., Kennedy, G.L., Burger, P., Friis, H., Jensen, A.M., Kanstrup, M., Bernasconi,

819   S.M., Thibault, N., Ullmann, C.V., and Vickers, M.L. Petrography and geochemical analysis of Arctic

820   ikaite   pseudomorphs   from   Utqiaġvik   (Barrow),   Alaska,   Norw.   J.   Geol.,   103,   202303.

821   https://dx.doi.org/10.17850/njg103-1-3, 2023.

822   Sluijs, A., Frieling, J., Inglis, G.N., Nierop, K.G., Peterse, F., Sangiorgi, F. and Schouten, S. Late

823   Paleocene–early Eocene Arctic Ocean sea surface temperatures: reassessing biomarker

824   paleothermometry at Lomonosov Ridge. Clim. Past, 16(6), 2381-2400. https://doi.org/10.5194/cp-16-

825   2381-2020, 2020.

826   Spielhagen, R.F. and Tripati, A. Evidence from Svalbard for near-freezing temperatures and climate

827   oscillations in the Arctic during the Paleocene and Eocene. Palaeogeogr. Palaeocl., 278(1-4), 48-56.

828   https://doi.org/10.1016/j.palaeo.2009.04.012, 2009.

829   Stockmann, G.J., Seaman, P., Balic-Zunic, T., Peternell, M., Sturkell, E., Liljebladh, B. and Gyllencreutz,

830   R. Mineral Changes to the Tufa Columns of Ikka Fjord, SW Greenland. Minerals, 12(11), 1430.

831   https://doi.org/10.3390/min12111430, 2022.

832   Stockmann, G., Tollefsen, E., Skelton, A., Brüchert, V., Balic-Zunic, T., Langhof, J., Skogby, H. and

833   Karlsson, A. Control of a calcite inhibitor (phosphate) and temperature on ikaite precipitation in Ikka

834   Fjord,   southwest   Greenland.   Appl.   Geochem.,   89,   11-22.

835   https://doi.org/10.1016/j.apgeochem.2017.11.005, 2018.

836   Stokke, E.W., Jones, M.T., Tierney, J.E., Svensen, H.H. and Whiteside, J.H. Temperature changes across

837   the Paleocene-Eocene Thermal Maximum–a new high-resolution TEX86 temperature record from the

838   Eastern North Sea Basin. Earth Planet. Sc. Lett., 544, 116388.

839   https://doi.org/10.1016/j.epsl.2020.116388, 2020a.

840   Stokke, E.W., Liu, E.J., Jones, M.T. Evidence of explosive hydromagmatic eruptions during the

841   emplacement of the North Atlantic Igneous Province. Volcanica, 3 (2), 227-250.

842   https://doi.org/10.30909/vol.03.02.227250, 2020b.

843   Suess, E., Balzer, W., Hesse, K.F., Müller, P.J., Ungerer, C.T. and Wefer, G. Calcium carbonate

844   hexahydrate from organic-rich sediments of the Antarctic shelf: precursors of glendonites. Science,

845   216(4550), 1128-1131. https://doi.org/10.1126/science.216.4550.1128, 1982.

846   Tollefsen, E., Balic-Zunic, T., Mörth, C.M., Brüchert, V., Lee, C.C. and Skelton, A., 2020. Ikaite nucleation

847   at 35 C challenges the use of glendonite as a paleotemperature indicator. Sci Rep.-UK, 10(1), 8141.

848   https://doi.org/10.1038/s41598-020-64751-5, 2020.

849   Torres, M.E., Marsaglia, K.M., Martin, J.B. and Murray, R.W. Sediment diagenesis in western Pacific

850   basins. Geoph. Monog., 88, 241-258., 1995.

851   Ullmann, C.V., Boyle, R., Duarte, L.V., Hesselbo, S.P., Kasemann, S.A., Klein, T., Lenton, T.M., Piazza, V.

852   and Aberhan, M. Warm afterglow from the Toarcian Oceanic Anoxic Event drives the success of deep-

853   adapted brachiopods. Sci Rep.-UK, 10(1), 6549. https://doi.org/10.1038/s41598-020-63487-6, 2020.

854   Vickers, M., Watkinson, M., Price, G.D. and Jerrett, R., 2018. An improved model for the ikaite-

855   glendonite transformation: evidence from the Lower Cretaceous of Spitsbergen, Svalbard. Norw. J.

856   Geol., 98(1), 1 – 15 https://dx.doi.org/10.17850/njg98-1-01, 2018.

857   Vickers, M.L., Price, G.D., Jerrett, R.M., Sutton, P., Watkinson, M.P. and FitzPatrick, M., 2019. The

858   duration and magnitude of Cretaceous cool events: Evidence from the northern high latitudes. Geol.

859   Soc. Am. Bull., 131(11-12), 1979-1994. https://doi.org/10.1130/B35074.1, 2019.

860   Vickers, M.L., Lengger, S.K., Bernasconi, S.M., Thibault, N., Schultz, B.P., Fernandez, A., Ullmann, C.V.,

861   McCormack, P., Bjerrum, C.J., Rasmussen, J.A. and Hougård, I.W. Cold spells in the Nordic Seas during

862   the early Eocene Greenhouse. Nat. Comm., 11(1), 4713. https://doi.org/10.1038/s41467-020-18558-

863   7, 2020.

864   Vickers, M.L., Vickers, M., Rickaby, R.E., Wu, H., Bernasconi, S.M., Ullmann, C.V., Bohrmann, G.,

865   Spielhagen, R.F., Kassens, H., Schultz, B.P. and Alwmark, C. The ikaite to calcite transformation:

866   Implications for palaeoclimate studies. Geochim. Cosmochim. Ac., 334, 201-216.

867   https://doi.org/10.1016/j.gca.2022.08.001, 2022.

868   Westerhold, T., Marwan, N., Drury, A.J., Liebrand, D., Agnini, C., Anagnostou, E., Barnet, J.S., Bohaty,

869   S.M., De Vleeschouwer, D., Florindo, F. and Frederichs, T. An astronomically dated record of Earth's

870   climate and its predictability over the last 66 million years. Science, 369(6509), 1383-1387.

871   https://doi.org/10.1126/science.aba6853, 2020.

872   Whiticar, M.J., Suess, E., Wefer, G. and Müller, P.J. Calcium carbonate hexahydrate (ikaite): History of

873   mineral formation as recorded by stable isotopes. Minerals, 12(12), 1627.

874   https://doi.org/10.3390/min12121627, 2022.

875   Zachos, J.C., Dickens, G.R. and Zeebe, R.E. An early Cenozoic perspective on greenhouse warming and

876   carbon-cycle dynamics. Nature, 451(7176), 279-283. https://doi.org/10.1038/nature06588, 2008.

877   Zacke, A., Voigt, S., Joachimski, M.M., Gale, A.S., Ward, D.J., Tütken, T. Surface-water freshening and

878   high-latitude river discharge in the Eocene North Sea. J. Geol. Soc. London, 166, 969-980.

879   https://doi.org/10.1144/0016-76492008-068, 2009.

880   Zhou, X., Lu, Z., Rickaby, R.E., Domack, E.W., Wellner, J.S. and Kennedy, H.A., 2015. Ikaite abundance

881   controlled by porewater phosphorus level: Potential links to dust and productivity. J. Geol., 123(3),

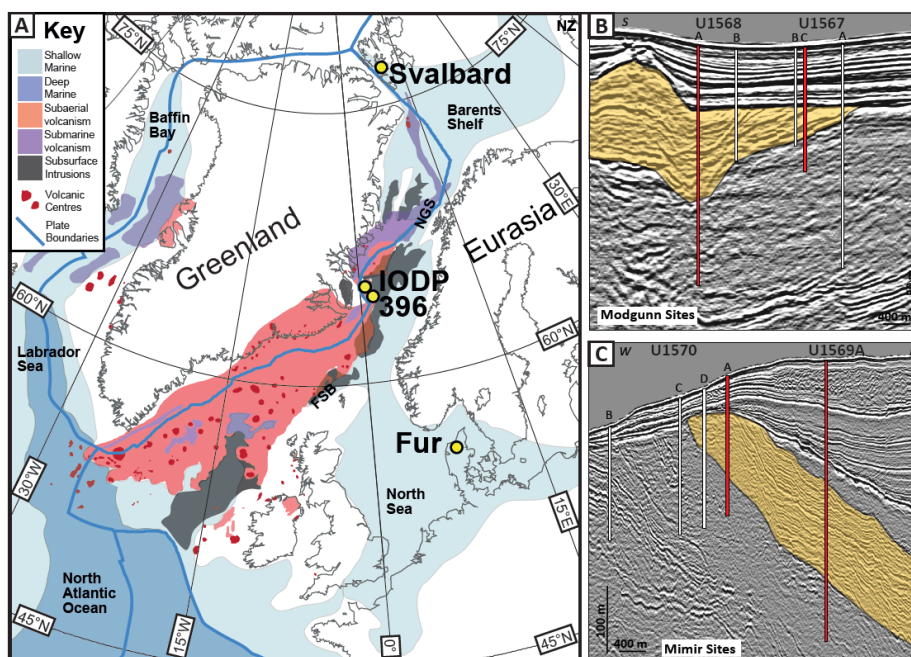882   269-281. https://doi.org/10.1086/681918, 2015.

883

Figure 1: (A) Paleogeographic map of the Nordic Seas region with North Atlantic Igneous Province volcanism shown, after Jones et al. (2023). Location of all known Paleocene – Eocene glendonite bearing sites marked – Exp. 396 Modgunn and Mimir cores (this study); Paleogene-Eocene sediments of Svalbard (Spielhagen and Tripati, 2009), and early Eocene Fur Formation of northern Denmark (Vickers et al., 2020). **(B)** High-resolution 3-D seismic data for holes 1568 and 1567 along the Modgunn transect (from Planke et al., 2023). **(C)** High-resolution 3-D seismic data for holes 1569 and 1570 along the Mimir Transect (from Planke et al., 2023). Holes from which glendonites were recovered are shown in red. PETM intervals are shown in yellow.

884

885

886

887

888

889
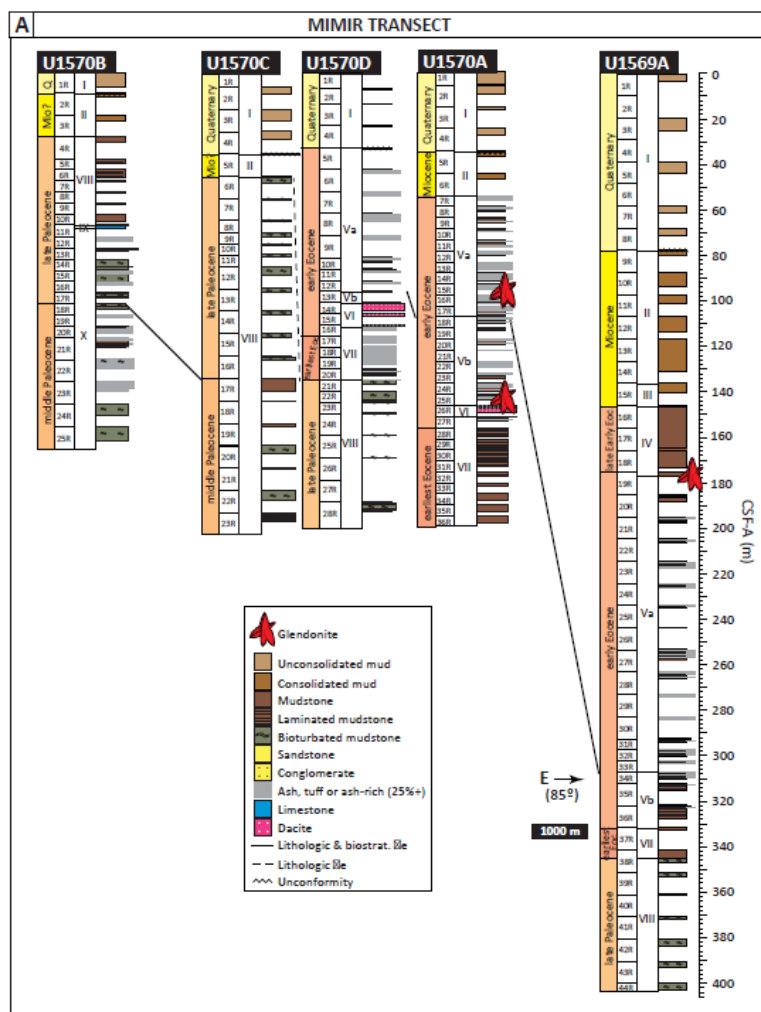
Figure 2: Overview logs of the cores with glendonite horizons marked by the red glendonite cartoon. (A) The Mimir (U1569 - U1570) transect, from Planke et al. (2023). For the correlations between cores, all ties (solid black lines) are supported by lithologic change and biostratigraphic zonation. The dashed line represents correlation by lithologic change within a biostratigraphic zone, aiming to tie Hole U1570C to Hole U1570D (Planke et al., 2023). (B) The Modgunn (U1567 - U1568) transect, from Planke et al. (2023). Core sections of PETM age are highlighted in yellow, and the hydrothermal vent infill (e.g. Fig. 1B) is shown in grey. All correlations between cores are supported by lithologic change, biostratigraphic zonation, and carbon isotope stratigraphy (Berndt et al., 2023).

890
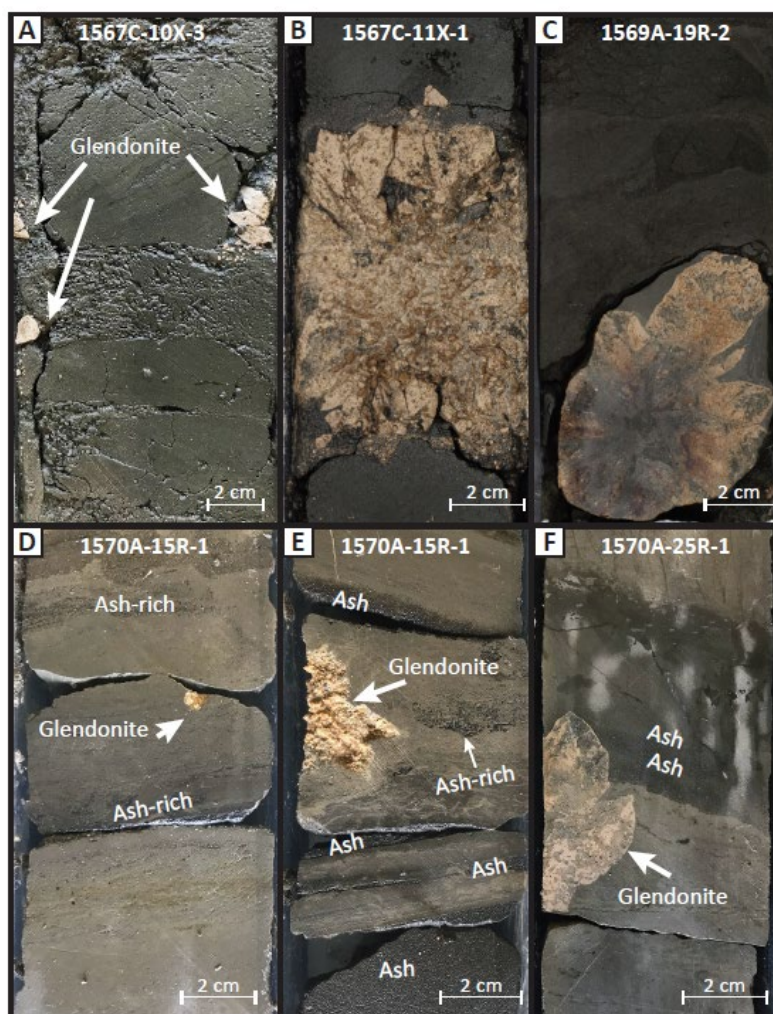
891

892

Figure 3: Photographs of glendonites *in situ* in the cores from the Modgunn and Mimir transects. **(A)** Glendonite fragments in drill mud from 1567C-10X-3 40-45 (MLV 86). **(B)** Glendonite from section 1567C-11X-1 94-95 (MLV 57, 97). **(C)** Cemented glendonite from section 1569A-19R-2 54-62 (MLV 90). **(D)** Glendonite from section 1570A-15R-1 108-112 (MLV 92). **(E)** Glendonite fragment in 1570A-15R-1 22-25 (MLV 91). **(F)** Glendonite from section 1570A-25R-1 (MLV 93).

893
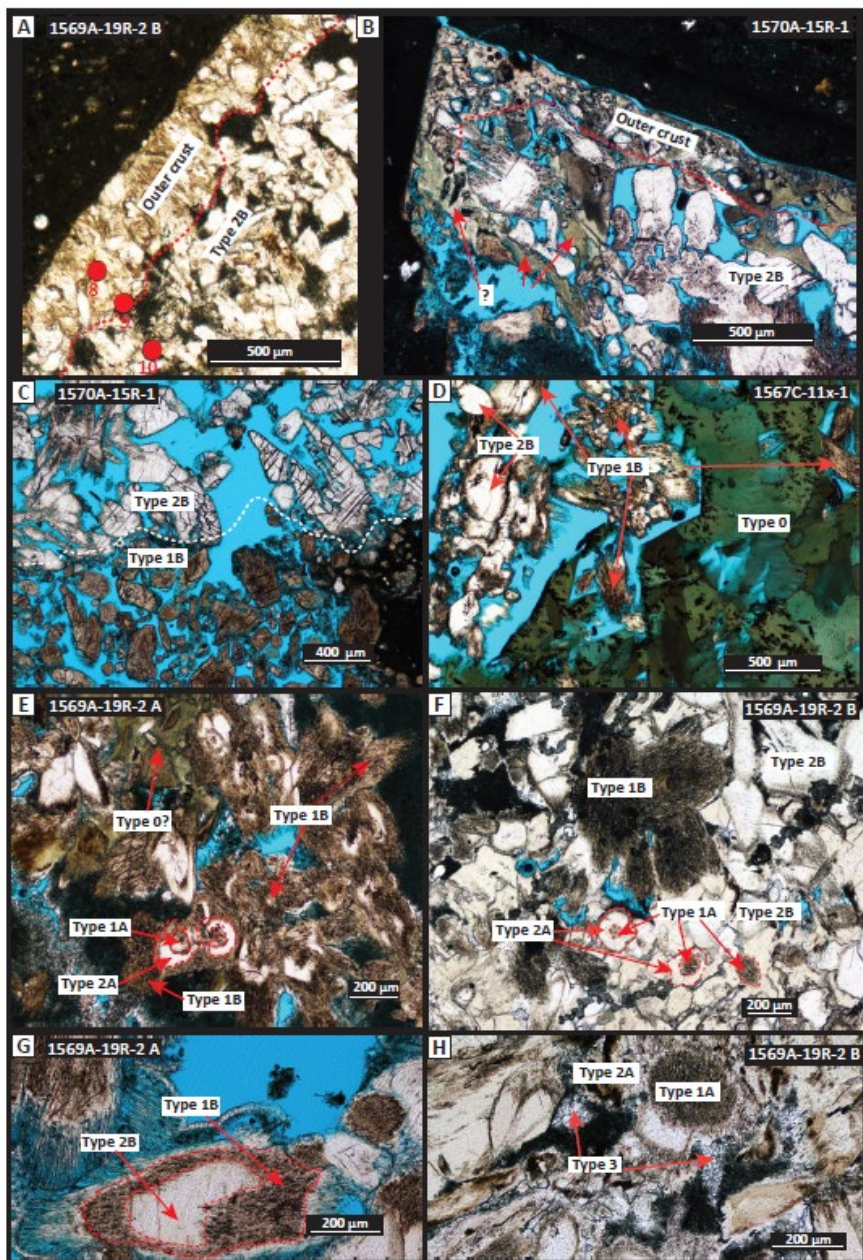
894

Figure 4: Photomicrographs of polished thin sections from selected Exp. 396 glendonites. The blue background colour is derived from the resin rather than the glendonite. **(A)** and **(B)** show the typical harder outer rim with more porous centre characteristic of transformed ikaite (e.g. Schultz et al., 2023). Red dots labelled 8, 9 and 10 are spots where LA ICP-MS analysis was performed. The glendonites commonly show areas of different calcite types defined by colour, which are often hard to place into the "traditional" carbonate phase types seen in other glendonites (e.g. Huggett et al., 2005; Vickers et al., 2018). **(C)** shows a distinct boundary between white Type 2B calcite and brown Type 1B calcite, neither of which show zoning defined by colour or porosity. **(D)** shows the sharp boundary between green Type 0 carbonate, with black dendritic surface growth, and other calcite phases. The shape of the sharp boundary that Type 0 defines on one side suggests that Type 0 grew on the surface of and out from an ikaite crystal, which later broke down to leave void space and patches of Type 1B with 2B overgrowths.

(E) and **(F)** show patches of more typical zoned calcite blebs, here labelled 1A and 2A, which appear to fit into the traditional categories of "Type I" (zoned brown calcite forming the centre of the blebs) and "Type II" (zoned pale overgrowths on Type I; e.g. Vickers et al., 2018; Schultz et al., 2023). **(G)** Apparent reversal of the "typical" glendonite fabric, whereby the central area of the calcite blebs is pale/white Type 2B and the overgrowth brown Type 1B calcite. This contrasts with **(H)** which shows dark Type 1A with white Type 2A overgrowths.
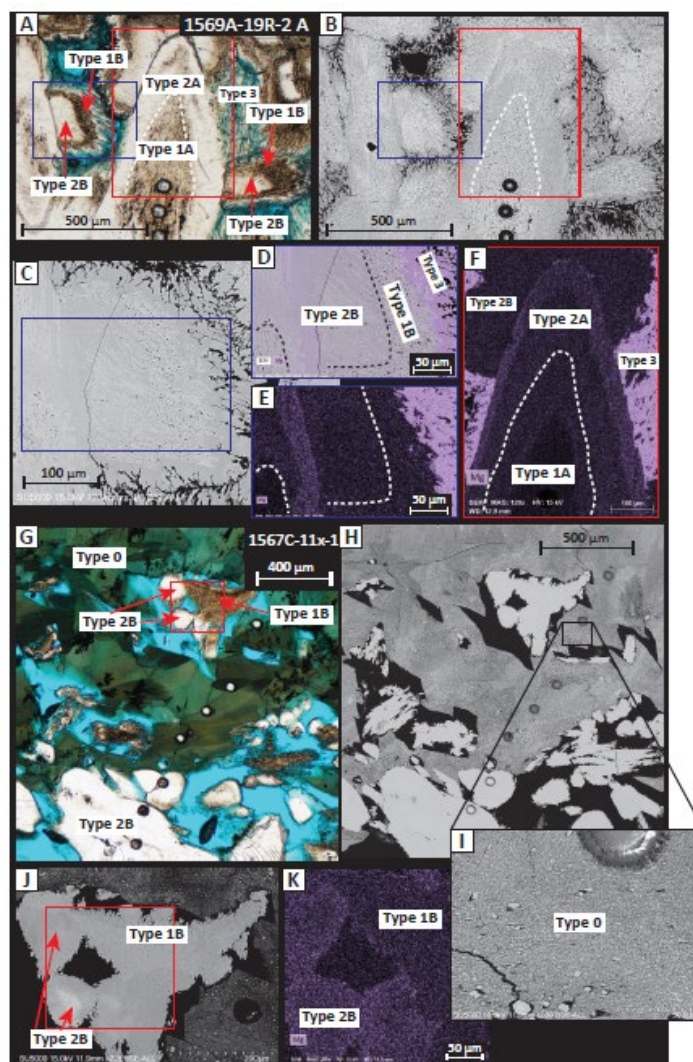
895

Figure 5: Light microscopy, SEM photomicrographs and EDS element maps from thin sections of glendonites at 1569A-19R-2 and 1567C-11X-1. **(A)** Overview under plane polarised light of the area examined for glendonite at 1569A-19R-2, with the carbonate phases labelled. **(B)** BSE image of the same area. Higher porosity in the Type 1 can be seen. **(C)** BSE image of zoomed in area of Type 2B with Type 1B overgrowth. Higher porosity of Type 1 is again clear. **(D)** EDS map showing Mg distribution across calcite types 1B and 2B, overlaid on the BSE photomicrograph. **(E)** The same map without the BSE photomicrograph **(F)** EDS map showing Mg distribution across calcite types 1A, 2A and 2B. **(G)** Overview under plane polarised light of the area examined for glendonite at 1567C-11X-1. **(H)** BSE image of the same area, with pop-out **(I)** showing the microcrystalline nature of Type 0. **(J)** Magnification of the same area with types IB and 2B calcite under BSE. **(K)** EDS element map showing the Mg distribution across the same area.
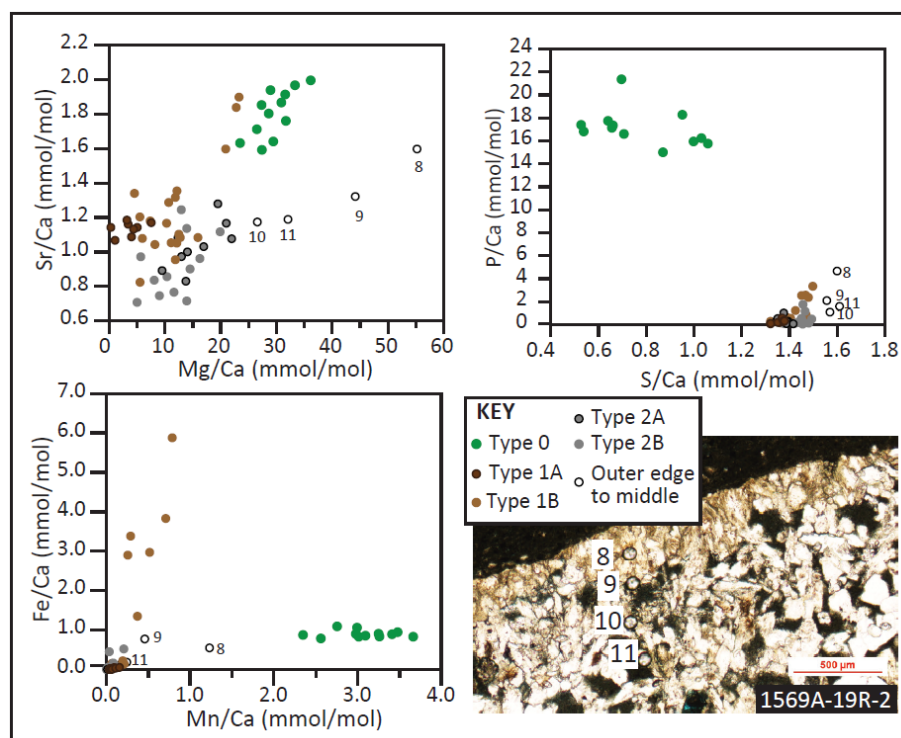
896

Figure 6: LA ICP-MS element/Ca data for points across the Exp. 396 glendonite polished thin sections. The data have been grouped according to the calcite types described in the main text and in the preceding figures. Photomicrograph showing the location points 8 – 11 from outer edge inwards are shown bottom right, and also in Fig. 4A. Photomicrographs showing the location of all the individual points measured may be found in the Supplementary Material.
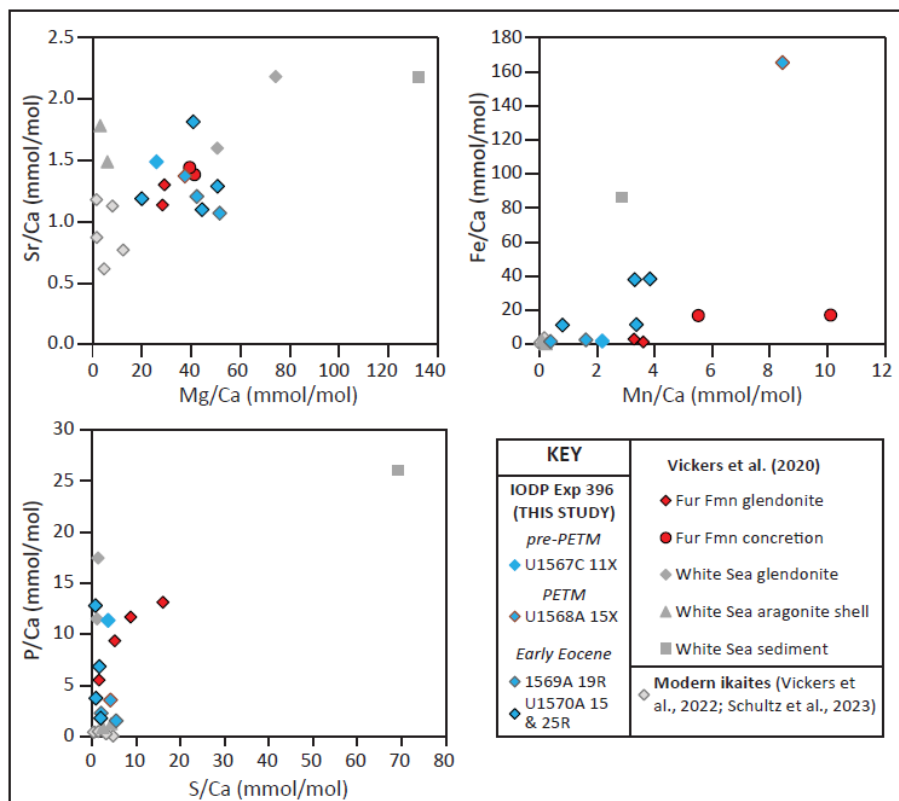
Figure 7: Element/Ca ratios of the Exp. 396 glendonites and associated calcites compared to published ICP-OES data for other glendonite-bearing sites.
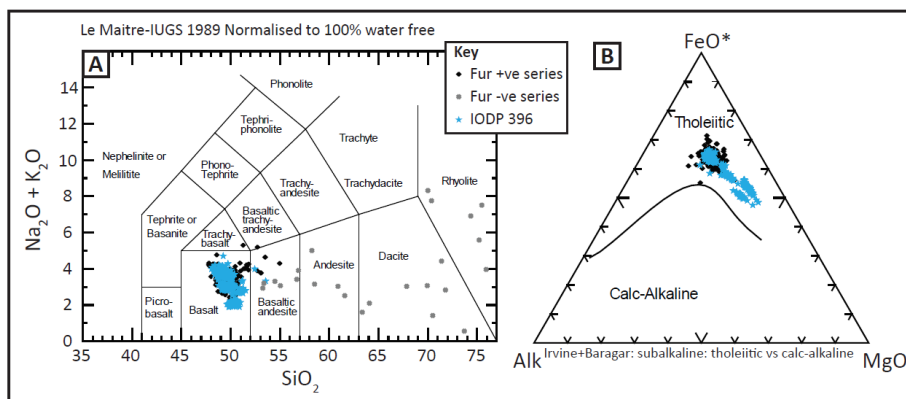
898

Figure 8: (A) A Total Alkali Silica (TAS) plot comparing the Exp. 396 ashes (this study) to published data for both positive (Stokke et al. 2020b) and negative (Larsen et al., 2003) ash series of the Fur Formation in northern Denmark. The Exp. 396 ashes and Fur positive series fall into the basaltic fields, whereas the Fur negative series show much more variation and have overall more felsic compositions. Note that while the Fur positive series data are microprobe analyses of matrix glass, the Fur Negative series data are whole rock data. However, the whole rock samples were leached of clay prior to analysis and no significant dilution is expected. **(B)** Ternary Alkali-Iron-Magnesium (AFM) diagram showing that the basaltic ashes from both the Exp. 396 sites and the Fur positive series are tholeiitic basalts. Note that many of the Exp. 396 ashes have higher MgO content than the Fur positive ashes.
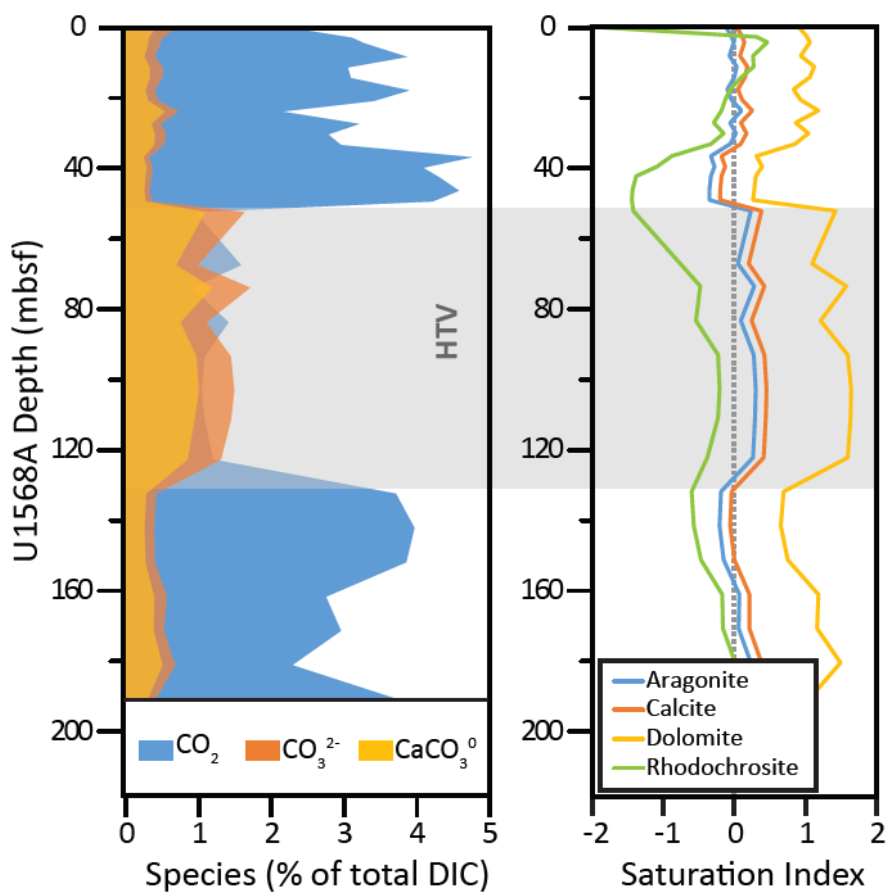
Figure 9: PHREEQC simulation results for the U1568A core, which spans the hydrothermal vent infill (grey highlight labelled 'HTV'). Note that HCO_3^- (the major species) is not shown.
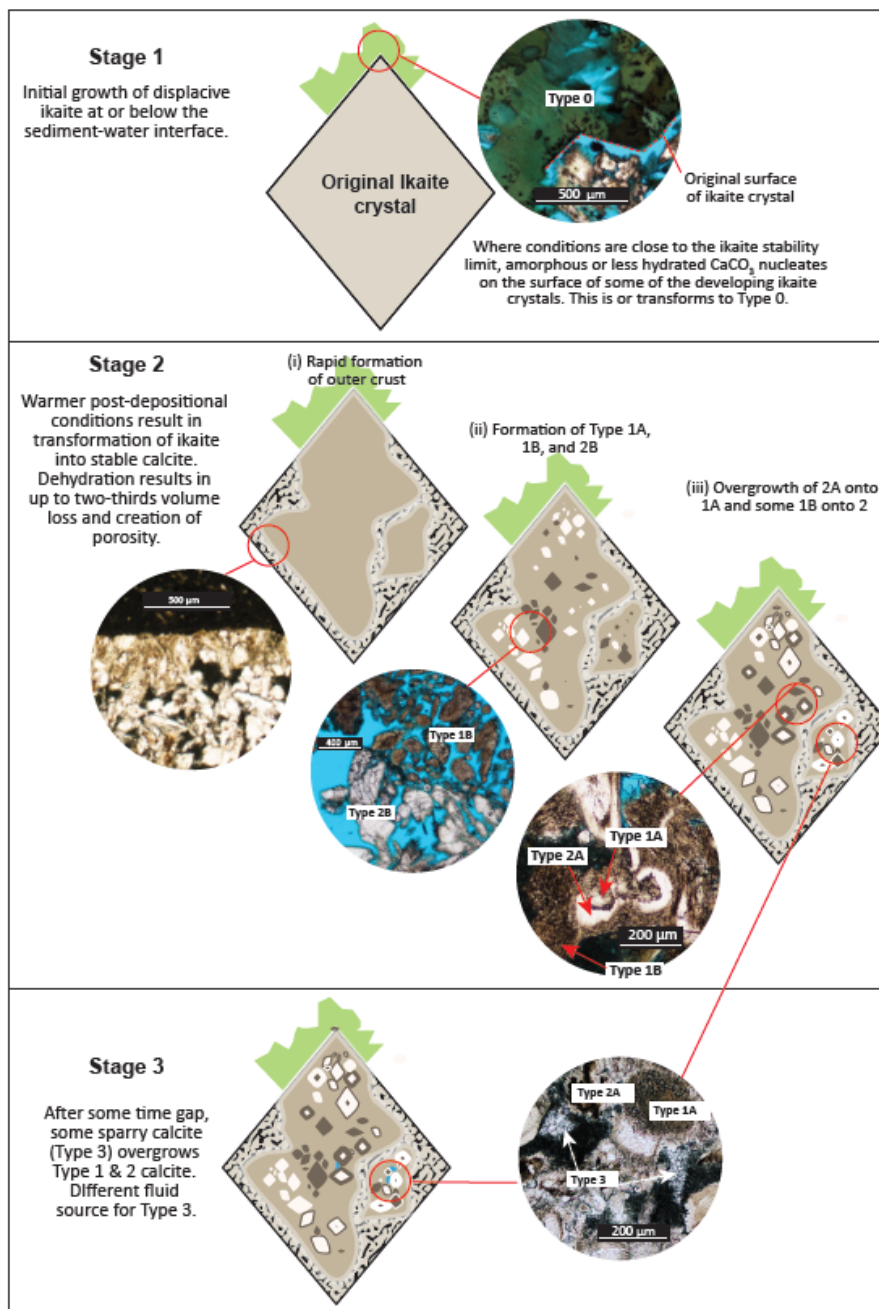
899

900

Figure 10: Schematic of ikaite transformation in the Exp. 396 cores, adapted from Counts et al. (*in review*) based on observed textural relationships and geochemistry of the calcite phases in the Exp. 396 glendonites.
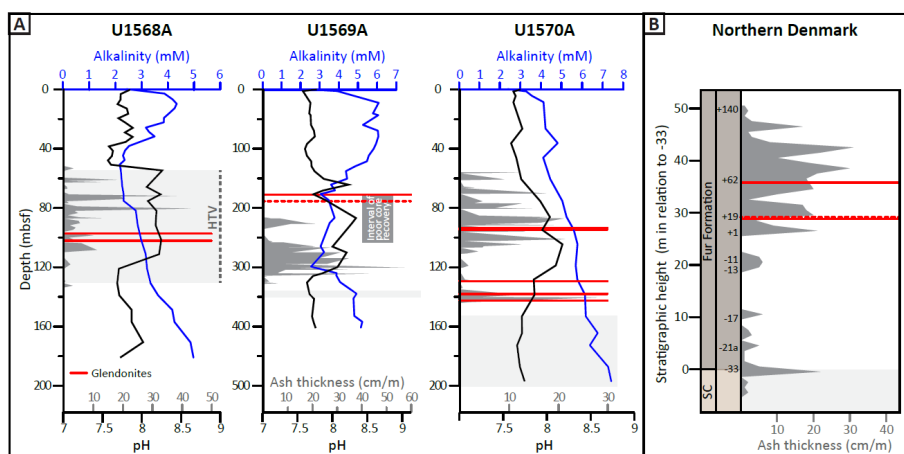
901

Figure 11: (A) Relative position of glendonites in the Paleocene-Eocene sediments of selected cores from the mid-Norwegian Margin, Exp. 396, compared to measured ash thicknesses. Pore water alkalinity and pH data (Planke et al., 2023) are also shown. Pale grey indicates the PETM-aged intervals in the stratigraphy. Note that for U1569A, core recovery was poor, particularly in the bottom, ash-bearing part (see Fig. 2). High ash contents lead to lower core recovery as they are course-grained and unlithified; therefore it is likely that there were much more numerous and thicker ash horizons in the interval between 18R and 37R (c. 180 – 340 mbsf). **(B)** Relative position of glendonites in the Paleocene-Eocene sediments of Northern Denmark, compared to ash thicknesses per metre (Jones et al., 2023). Glendonite horizons for the Fur Formation are from Vickers et al., (2020) (solid lines) and dashed line as identified by Henrik Friis, pers. comm. Pale grey indicates the end of the body of the PETM carbon isotope excursion (Jones et al., 2023). The recovery phase is between ashes -33 and -21a. SC = Stolleklint Clay.

902

Site	Hole	Core	Core type	Section	Top depth (cm)	Bottom depth (cm)	mbsf top	PXRD mineralogy	Remarks
1567	C	10	X	3	40	45			Displaced (in drill mud)
1567	C	11	X	1	83	93	82.03	Calcite, minor halite, Qz	Not cemented
1568	A	15	X	1	29	31	97.3		Porous calcite in cement
1568	A	15	X	4	49	51	102.0		Not cemented
1568	A	15	X	4	55	58	102.1	Calcite, minor Qz, rhodochrosite	Not cemented
1569	A	19	R	2	54	62	177.3	Calcite, Mg-calcite, minor Qz, gypsum, halite	Partially cemented
1570	A	15	R	1	22	25	93.6		Not cemented. Small fragment
1570	A	15	R	1	108	112	94.5	Calcite, minor Qz + halite	Not cemented, half glendonite
1570	A	22	R	2	89	91	129.3		Cemented glendonite fragment (tip of crystal)
1570	A	24	R	1	96	98	138.1		Uncemented glendonite fragments
1570	A	25	R	1	50	55	142.5	Calcite, minor Mg-calcite, Qz	Cemented (in lmst)

Table 1: Glendonites of the Exp. 396 cores, PXRD data from bulk glendonite analysis, element/Ca ratios.

903

Carbonate phase	Description
Type 0	Green-brown carbonate phase, not observed in all glendonites (Fig. 4). Heterogeneous colour distribution from browner to greener areas, not visibly zoned under plane polarised light (Fig. 4B and F). Commonly shows black dendritic surface patterns. SEM imaging revealed Type 0 to be composed of micro-grains of carbonate, rather than being a single crystal (Fig. 5).
Type 1A	Forms dark brown, zoned, with zoned overgrowths of paler calcite (Fig. 4). The BSE SEM shows it has higher porosity than the calcite overgrowths, and EDS mapping shows some chemical zoning defined by its Mg concentration (Fig. 5). Equivalent to Type 1 (I) of Huggett et al. (2005), Vickers et al. (2018), Schultz et al. (2023), and Counts et al. (*in review*).
Type 1B	Uneven colour from brown to dark brown. Generally overgrows, or intergrows with pale, non-porous Type 2A. Type 1B is indistinguishable from Type 1A except that it grows over Type 2A rather than the other way around, and generally has slightly higher [Mg] than 1A. Type 1B is not visibly zoned, and makes up larger patches/areas (Fig. 4 C – F; Fig. 5).
Type 2A	White calcite (under plane polarised light) that directly overgrows Type 1A, showing Mg-zoning (Fig. 4), and generally higher Mg than Type 1A (Fig. 5). Low/no porosity compared to Type 1A&B (Fig. 5). Equivalent to Type 2 (II) of Huggett et al. (2005), Vickers et al. (2018) and Schultz et al. (2023) and Type 2A of Counts et al. (*in review*).
Type 2B	Very similar to Type 2A, white, homogenous calcite with no colour or porosity zoning; but unlike 2A also lacking chemical zoning (Fig. 5). Type 2B calcite is generally characterised by a higher Mg than Type 1A&B calcite phases (Fig 5).
Type 3	Isopachous sparry or fibrous epitaxial calcite overgrowths to Types 1 and 2; higher [Mg] than types 1 and 2 (Figs. 4H and 5).

Table 2: Descriptions of the different carbonate phases observed within the glendonites through thin section microscopic and geochemical analysis (light microscopy, SEM, EDS and LA-ICP-MS).